NAM

Unbiased Cyclic Resistance Ratio Relationships for Evaluating Liquefaction Potential in Groningen

Russell Green, Julian Bommer, Adrian Rodriguez-Marek & Peter Stafford

Datum June 2016

Editors Jan van Elk & Dirk Doornhof

General Introduction

The soils in Groningen contain deposits of saturated sands. Therefore the possibility of earthquake-induced liquefaction also needs to be considered. In particular, liquefaction could potentially be important for critical infra-structure like dikes and levees.

Existing methods for the evaluation of liquefaction triggering were developed using liquefaction observations for large magnitude earthquakes. While most of the recently proposed liquefaction triggering evaluation procedures yield similar results for scenarios that are well represented in the liquefaction case history databases, their predictions deviate for other scenarios (e.g., low magnitude events, very shallow and very deep liquefiable layers, high fines content, medium dense to dense soils). These deviations can be significant enough that the results from one evaluation procedure may indicate that risk from liquefaction is low, while another procedure may indicate that the risk is high. These methods for evaluating liquefaction triggering might therefore not be appropriate for use in the Groningen conditions.

The recent earthquakes around Canterbury, New Zealand, have extended this liquefaction case history database with many well documented liquefaction case histories, relevant to the Groningen situation. Extending the database with the New Zealand liquefaction case histories and re-analyzing the case histories in the already existing database, allowed development of a methodology for evaluation of liquefaction triggering more appropriate for the Groningen conditions. This method is described in this report.

However, while the new methodology described in this report is suitable for estimating the liquefaction resistance on the soils in the Groningen region, region-specific relationships appropriate for estimating the seismic demand imposed on the soil from induced earthquakes in Groningen need to be developed; this work is ongoing.

NAM

Title	**Unbiased Cyclic Resistance Ratio Relationships for Evaluating Liquefaction Potential in Groningen.**		**Date**	June 2016
			Initiator	NAM
Author(s)	Russell Green, Julian Bommer, Adrian Rodriguez-Marek & Peter Stafford.	**Editor**	Jan van Elk Dirk Doornhof	
Organisation	Team of Academic Experts	**Organisation**	NAM	
Place in the Study and Data Acquisition Plan	Study Theme: Liquefaction Comment: The soils in Groningen contain deposits of saturated sands. Therefore the possibility of earthquake-induced liquefaction also needs to be considered. In particular, liquefaction could potentially be important for critical infra-structure like dikes and levees. Existing methods for the evaluation of liquefaction triggering were developed using liquefaction observations for large magnitude earthquakes. While most of the recently proposed liquefaction triggering evaluation procedures yield similar results for scenarios that are well represented in the liquefaction case history databases, their predictions deviate for other scenarios (e.g., low magnitude events, very shallow and very deep liquefiable layers, high fines content, medium dense to dense soils). These deviations can be significant enough that the results from one evaluation procedure may indicate that risk from liquefaction is low, while another procedure may indicate that the risk is high. The recent earthquakes around Canterbury, New Zealand, have extended this liquefaction case history database with many well documented liquefaction case histories relevant to the Groningen situation. Extending the database with the New Zealand liquefaction case histories and re-analyzing the case histories in the already existing database, allowed development of a methodology for evaluation of liquefaction triggering more appropriate for the Groningen conditions. This method is described in this report. However, while the new methodology described in this report is suitable for estimating the liquefaction resistance on the soils in the Groningen region, region-specific relationships appropriate for estimating the seismic demand imposed on the soil from induced earthquakes in Groningen need to be developed; this work is ongoing.			
Directly linked research	1. Site Response of shallow subsurface and soils. 2. Ground Motion Prediction.			

Used data	liquefaction case history databases extended with liquefaction case histories from recent earthquakes near Canterbury, New Zealand.
Associated organisation	Department of Civil and Environmental Engineering at Virginia Tech, Virginia, USA.
Assurance	This research has been published in peer-reviewed papers.

Unbiased Cyclic Resistance Ratio Relationships for Evaluating Liquefaction Potential in Groningen

Russell Green
Julian Bommer
Adrian Rodriguez-Marek
Peter Stafford

3 April 2016

Contents

1. Introduction and Background 2

2. Stress Reduction Coefficient, r_d 3
2.1 Ground motions used to develop stress reduction coefficient, r_d 6
2.2 Soil profiles used to develop stress reduction coefficient, r_d 7
2.3 Stress reduction coefficient, r_d 7
2.4 Comparison with other stress reduction coefficient, r_d, relationships 9

3. Magnitude Scaling Factors, MSF 10
3.1 Accounting for multi-directional shaking 16
3.2 n_{eq} correlation 17
3.3 b-value used to compute MSF 19
3.4 Magnitude Scaling Factors, MSF 22

4. Combined Influence of New r_d and MSF Relationships 31
4.1 Efficacy of the new r_d and MSF relationships in combination 31
4.2 Impact of new rd and MSF relationships on liquefaction predictions 34

5. Unbiased Probabilistic CRR Relationship 39

6. Summary 42

7. References 44

Appendices

A. Ground Motions Used to Develop New r_d and MSF Relationships 47

1. Introduction and Background

Gas production in the Groningen field is causing induced earthquakes, in response to which NAM is modelling the resulting hazard of ground shaking and the consequent risk to buildings in the region. Since there are widespread deposits of saturated sands in the region, the possibility of earthquake-induced liquefaction also needs to be considered. This need has been accentuated by various studies, proposals and online documents that have indicated a very severe liquefaction hazard, despite the small-to-moderate magnitudes of the earthquakes expected to occur. Because of the high profile that has been given to this hazard and also because of the potential impact on key infrastructure and lifelines—and in particular dikes—the Hazard and Risk Team (H&RT) is including the development of a model for the assessment of liquefaction hazard within its scope of work. The model for the assessment of the liquefaction hazard in the Groningen field is being developed by a joint collaboration between the H&RT and Deltares.

While most of the recently proposed liquefaction triggering evaluation procedures yield similar results for scenarios that are well represented in the liquefaction case history databases (*e.g*., Green *et al*., 2014), their predictions deviate for other scenarios (*e.g.*, low magnitude events, very shallow and very deep liquefiable layers, high fines content, medium dense to dense soils). These deviations can be significant enough that the results from one evaluation procedure may indicate that risk from liquefaction is low, while another procedure may indicate that the risk is high. Analysis of fifty well-documented liquefaction case histories from the 2010-2011 Canterbury, New Zealand, earthquake sequence showed that of the three commonly used CPT-based simplified liquefaction evaluation procedures (*i.e*., Robertson & Wride, 1998; Moss *et al*., 2006; Idriss & Boulanger, 2008), Idriss & Boulanger (2008) performed better than the others. The same conclusion was obtained from the analysis of several thousand case studies from the Canterbury earthquake sequence, wherein the procedures were used in conjunction with the LPI framework (Iwasaki *et al.*, 1978) to evaluate the severity of surficial liquefaction manifestations (Maurer *et al*., 2015a).

Despite the conclusions from the comparative studies using the New Zealand data, the Idriss & Boulanger (2008) procedure (and its successor, Boulanger & Idriss, 2014) is not suitable for direct use to evaluate liquefaction in Groningen. This is because of issues with r_d and MSF used in the procedure to compute CSR. The issues with r_d and MSF are systemic to the Idriss & Boulanger (2008) and Boulanger & Idriss (2014) procedures and cannot be simply corrected for (elaborated on subsequently). These issues are particularly significant for Groningen because the earthquakes induced from the gas extraction operations have small magnitudes and the associated motions have very different characteristics than those from tectonic earthquakes. Another limitation of the Idriss & Boulanger (2008) procedure is that it is deterministically formulated, not probabilistically. Although the more recent update of this approach (Boulanger & Idriss, 2014) is formulated probabilistically, the r_d relationship in this version of the procedure is the same as that used in the 2008 version. Additionally, the new MSF inherent to the Boulanger & Idriss (2014) procedure also has limitations. Hence, systemic issues exist in both procedures.

Because the issues with r_d and MSF used in both the Idriss & Boulanger (2008) and Boulanger & Idriss (2014) procedures are systemic, they cannot be simply corrected for. Rather, the case histories compiled by Boulanger & Idriss (2014) had to be re-analysed using appropriate r_d and MSF relationships and a new, unbiased CRR curve developed; however, unbiased r_d and MSF relations had to first be developed. This report presents the results of this effort. In the following sections, detailed overviews of the new r_d and MSF relationships are presented, and new unbiased CRR relationships are presented. However, while the new CRR relationships proposed herein are suitable for estimating the liquefaction resistance on the soils in the Groningen region, region-specific r_d and MSF relationships appropriate for estimating the seismic demand imposed on the soil from induced earthquakes in Groningen need to be developed; this work is ongoing.

2. Stress Reduction Coefficient, r_d

The stress reduction coefficient, r_d, is an empirical factor that accounts for the non-rigid response of the soil profile and is illustrated in Figure 1. Both the Idriss & Boulanger (2008) and the Boulanger & Idriss (2014) procedures use an r_d relationship that is biased in that it predicts overly high CSR values at depth in a soil profile. This bias is illustrated in Figure 2 and is pronounced for depth between ~3 to 20 m below the ground surface. This over-prediction may have initially been intentional under the premise that when the procedures were used in forward analyses to evaluate a site's liquefaction potential, they will yield "conservative" results (*i.e.*, an over estimation of the CSR). However, when used to evaluate case histories to develop the CRR curves that are central to both versions of the procedure, the biased r_d relationship actually results in an "unconservative" positioning of the CRR curves (*i.e.*, the CRR curves yield a higher estimated liquefaction resistance of the soil than is warranted).The significance of this issue is mitigated to some extent when the same r_d relationship used to develop the CRR curve is also used in forward analyses (*i.e.*, the bias tends to cancels out). However, this is not the case if site-specific r_d relationships developed from site response analyses are used in conjunction with CRR curves that were developed using a biased r_d relationship.

A new (unbiased) relationship for r_d was developed using an approach similar to that used by Cetin (2000). Equivalent linear site response analyses were performed on 50 soil profiles compiled by Cetin (2000) that are representative of those in the liquefaction case history databases (*i.e.*, Figure 3). However, a larger set of recorded input motions were used in these analyses than were available at the time Cetin (2000) performed his study. Statistical analysis of the site response results were used to develop two variants of the r_d relationship that allow it to be used when a profile's shear wave velocities are either known or unknown. As with all r_d relationships proposed to date, the relationships developed herein are the result of a pragmatic compromise between having a relationship that is simple in form and one that is able to compute stresses at depth in geologically complex profiles with little uncertainty. Accordingly, site-specific site response analyses should be performed to compute stresses in a profile for which it is

expected that large strain concentrations will occur in a given stratum (*e.g.*, large reversal is small strain shear wave velocity at a given depth); this is in lieu of using an r_d relationship to estimate stresses induced in the soil profile.

In the following, brief descriptions of the earthquake motion database and the soil profiles used to develop the r_d relationships are given. Next, the developed r_d relationships are presented, followed by a comparison with commonly used relationships.

CSR for induced at the base of a non-rigid soil column:

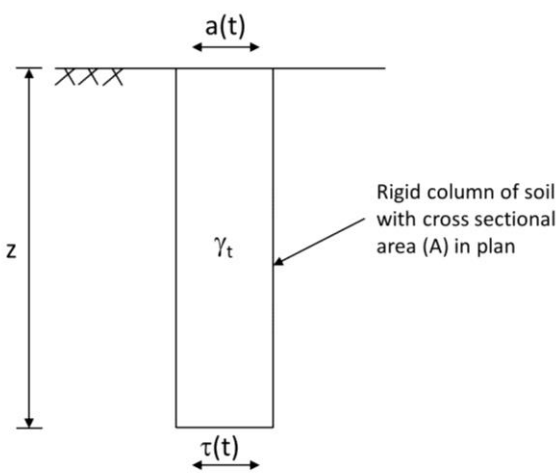

$$F(t) = m \cdot a(t)$$

$$= z \cdot A \cdot \frac{\gamma_t}{g} \cdot a(t)$$

$$\tau_{rigid}(t) = \frac{F(t)}{A} = \frac{a(t)}{g} \cdot \sigma_v$$

$$\tau_{rigid\ avg} = 0.65 \cdot \tau_{rigid\ max}$$

$$= 0.65 \cdot \frac{a_{max}}{g} \cdot \sigma_v$$

$$r_d = \frac{\tau_{non\text{-}rigid\ avg}}{\tau_{rigid\ avg}}$$

$$CSR = 0.65 \cdot \frac{a_{max}}{g} \cdot \frac{\sigma_v}{\sigma'_{vo}} \cdot r_d$$

F(t) = inertial force in rigid soil column induced by earthquake shaking
m = mass of soil column of having a cross-sectional area A and length z
a(t) = time dependent earthquake acceleration at the surface of the soil profile
γ_t = total unit weight of soil
g = coefficient of acceleration due to gravity
σ_v = total vertical stress at the base of the soil column
σ'_{vo} = effective vertical stress at the base of the soil column
a_{max} = peak ground acceleration at the surface of the soil profile
$\tau_{rigid}(t)$ = time dependent earthquake-induced shear stress at the base of a rigid soil column
$\tau_{rigid\ avg}$ = "average" earthquake-induced shear stress at the base of a rigid soil column
$\tau_{non\text{-}rigid\ avg}$ = "average" earthquake-induced shear stress at the base of a non-rigid soil column

Figure 1. The simplified stress-based liquefaction evaluation procedure quantifies the seismic demand imposed on the soil at depth *z* in terms of cyclic stress ratio (CSR). To account for the the non-rigid response of the soil profile, an empirical factor, r_d, is introduced. r_d is equal to the ratio of induced shear stress at depth *z* in a soil column determined from equivalent linear site response analyses to the ratio of shear stress at the base of a rigid soil column determined from Newton's second law of motion.

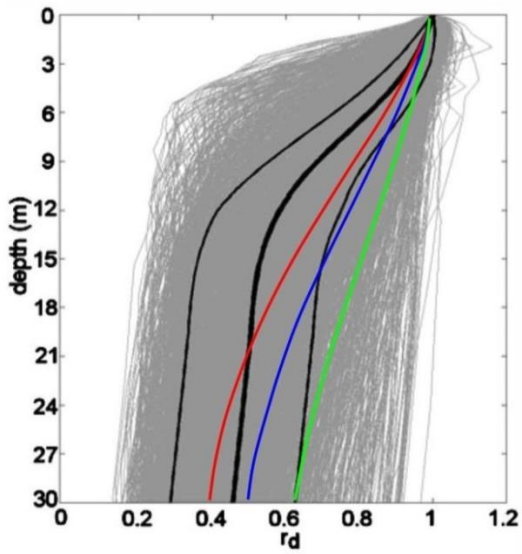

Figure 2. r_d factor used to account for the non-rigid response of the soil column. The grey lines were computed by Cetin (2000) from equivalent linear site response analyses performed using a matrix of 50 actual soil profiles and 40 recorded and scaled ground motions and two synthetic motions for **M** 8 strike slip and reverse events. The black lines are the median (thick line) and median plus/minus one standard deviation (thin lines) for the Cetin (2000) analyses. The red, blue, and green lines were computed using the r_d relation used in Idriss & Boulanger (2008) for **M** 5.5, **M** 6.5, and **M** 7.5 events, respectively.

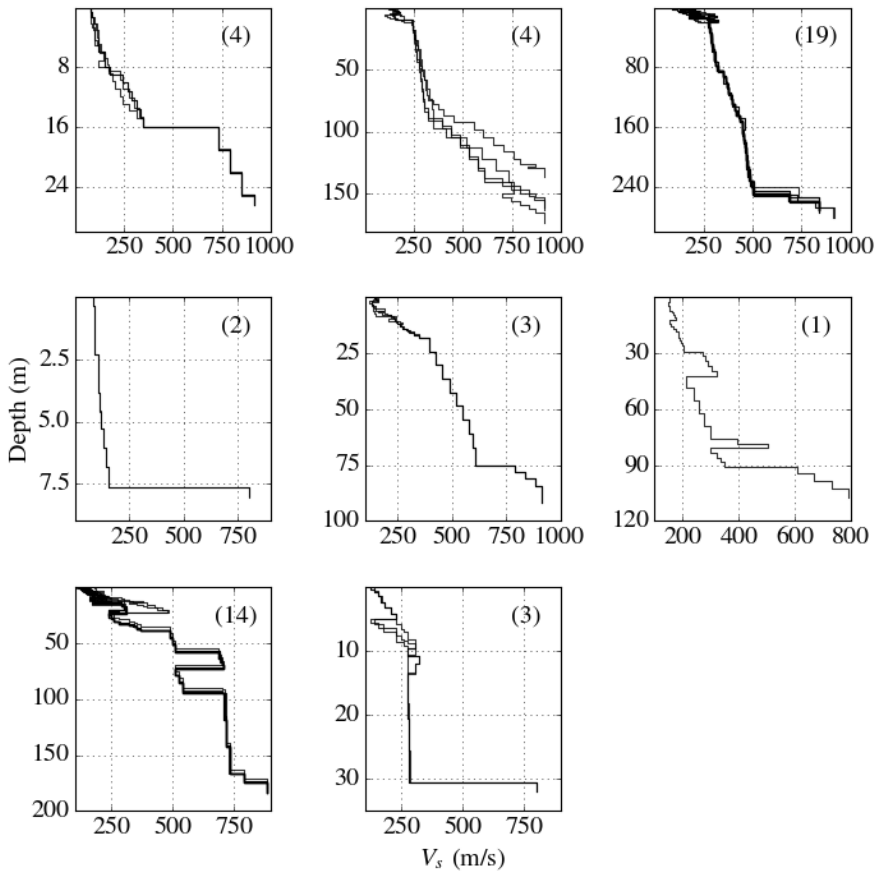

Figure 3. Soil profiles representative of those in the liquefaction case history data base. The number in the corner of each subplot is the number of profiles in the groupings of profiles having similar characteristics. (Lasley *et al.*, 2016)

2.1 *Ground motions used to develop stress reduction coefficient, r_d*

The earthquake motions used in the site response analyses to develop the r_d relationships came from the PEER NGA strong motion database (Chiou *et al.*, 2008), which is composed of 3551 multi-component records from 173 shallow crustal earthquakes. Of these 3551 records, 195 pairs of horizontal rock motions recorded during 47 earthquakes were used. The average shear wave velocities of the upper 30 m (V_{S30}) of all sites where the motions were recorded are greater than 650 m/s. The earthquake magnitudes associated with the motions range from 4.9 to 7.9, and site-to-source distances (closest distance from the recording site to the fault rupture plane) range from 1.5 to 295.4 km. These shallow crustal earthquake motions are representative of those associated with the cases histories in the liquefaction case history databases (*e.g.*, Boulanger & Idriss, 2014).

Table A1 in Appendix A list the motions used in the analyses. Also, Figure 4 shows the distribution of earthquake events as a function of magnitude and site-to-source distance. (Note that 34 pairs of motions, mostly from smaller magnitude events, used to

develop the new r_d are not plotted in Figure 4 because the site-to-source distances for these motions were unknown.)

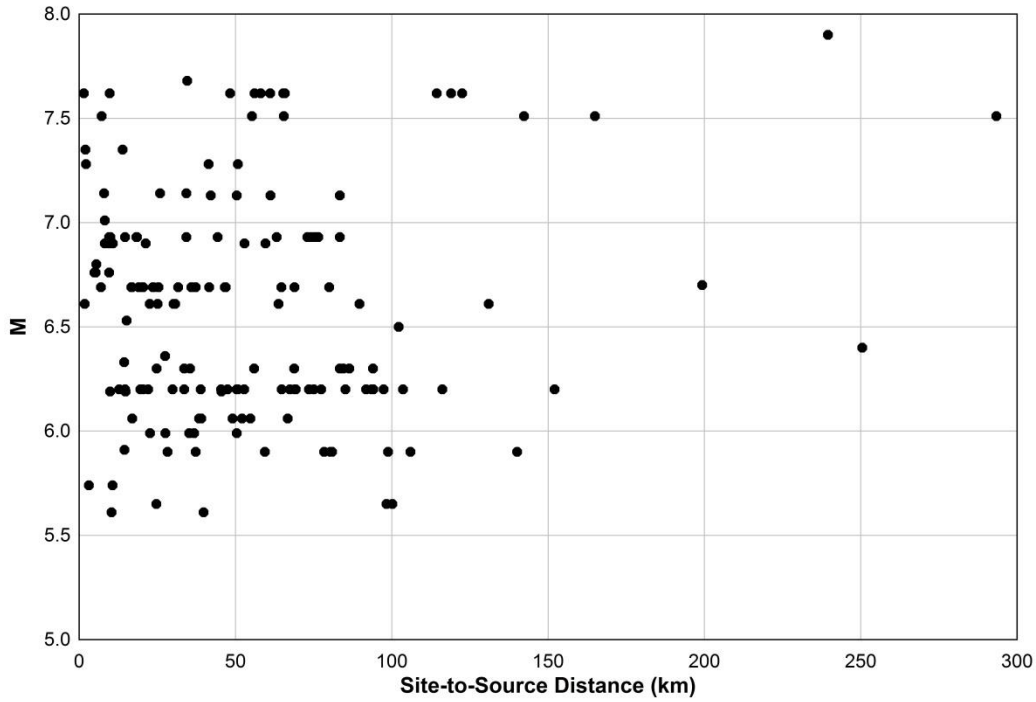

Figure 4. Magnitude versus distance distribution of the motions used in the site response analyses to develop the new r_d relationships. Each point in the plot represents a set of two horizontal motions; the site-to-source distances for several sets of motions used were not known and thus are not shown in this plot.

2.2 *Soil profiles used to develop stress reduction coefficient, r_d*

The soil profiles used in the site response analyses were compiled by Cetin (2000). The 50 well-characterized profiles are from post-earthquake site investigations in California and are shown in Figure 3. For each profile, Cetin provides a qualitative description of the layers (*e.g.,* clay, fine sand) and the shear wave velocities. Additional soil layer properties (unit weight, plasticity index, and at-rest lateral earth pressure coefficient) were randomly selected from a distribution of probable values corresponding to the qualitative description. Several of the profiles had similar characteristics, and the results from the site response analyses for these profiles were grouped for the regression analyses (discussed next), as shown in Figure 3.

2.3 *Stress reduction coefficient, r_d*

Several functional forms for r_d were examined in regressing the results from the site response analyses, and the following form was selected because of its simplicity and shape (*i.e.*, relatively low standard deviation of the regressed data):

$$r_d = (1-\alpha)exp\left(\frac{-z}{\beta}\right) + \alpha \quad (1)$$

where α is the limiting value of r_d at large depths and can range from 0 to 1. The variable β controls the curvature of the function at shallow depths, and *z* is the depth in meters. The term (1-α) scales the exponential so that r_d is equal to one at the ground surface.

For each combination of profile group and earthquake event, values of α and β were obtained using a non-linear least-squares curve-fitting algorithm (Jones *et al.*, 2001). From the results of the curve-fitting algorithm, regressions were performed to predict α and β using magnitude (**M**), peak ground acceleration at the surface of the profile (a_{max}), average shear wave velocity in the upper 12 meters of the profile (V_{S12}), V_{S30}, and closest distance to the fault rupture plane (R). Of these predictors, **M** and V_{S12} were found to be most strongly correlated with α and β. Although it was initially expected that α and β would show a strong correlation with shaking intensity, as represented by a_{max} (*e.g.*, Cetin *et al.*, 2004), statistically this was found not to be the case. The likely reason for this is that a_{max} is for the motions at the ground surface, not for those at the base rock. As a result, a relatively small a_{max} at the ground surface, for example, may be the result of a low intensity base rock motion and a relatively linear response of the soil profile (*i.e.*, small induced shear strains and low damping) or from a high intensity base rock motion and a highly non-linear response of the soil profile (*i.e.*, large induced shear strains and high damping). Although a_{max} for the ground surface motions are the same for these two scenarios, the corresponding r_d profiles would be very different.

Two different sets of expressions for α and β were developed, one set being a function of **M** and V_{S12} and the other being solely a function of **M**. This allows the use of the r_d relationship for profiles having varying levels of characterization. The first set of expressions for α and β is:

$$\alpha_1 = exp(b_1 + b_2\boldsymbol{M} + b_3 V_{s12}) \quad (2a)$$

$$\beta_1 = exp(b_4 + b_5\boldsymbol{M} + b_6 V_{s12}) \quad (2b)$$

and the second set is:

$$\alpha_2 = exp(b_1 + b_2\boldsymbol{M}) \quad (3a)$$

$$\beta_2 = b_3 + b_4\boldsymbol{M} \quad (3b)$$

where b_1-b_6 are regression coefficients.

While the functional forms of the above two sets of expressions were developed using the least-squares curve fitting, the regression coefficients (Table 1) were obtained by maximizing the likelihood, *L*, defined as:

$$L = \sum \left[ln\left(\frac{1}{\sigma\sqrt{2\pi}}\right) - \frac{(r_{d,Predicted} - r_{d,Actual})^2}{2\sigma^2} \right] \quad (4)$$

where σ is an error parameter regressed as part of the likelihood maximization and is defined as:

$$\sigma = b_7/(1 + exp(b_8 * z)) \quad (5)$$

b_7 and b_8 are additional regression coefficients, and z is as defined for Eq. 1. The regression coefficients were computed using a bootstrapping technique. A large number of points (10,000) were sampled (with replacement) from data corresponding to depths less than or equal to 20 m. Using this random sample, regression coefficients were obtained by maximizing the likelihood in Eq. 4. This process was repeated multiple times (1,000). Table 1 shows the mean values of the coefficients from all the iterations. As with any empirical relationship, care should be used when applying these equations for conditions outside the ranges from which they were regressed (*i.e.*, **M**: 5.3 to 7.6 and V_{S12}: 130 to 220 m/s). In particular, erroneous values will result when β is less than or equal to zero.

Table 1. Regression coefficients for the r_d relationships

Form	b_1	b_2	b_3	b_4	b_5	b_6	b_7	b_8
1	-3.793	0.4016	-0.001405	-1.380	0.3276	0.01332	0.1473	-0.4111
2	-4.373	0.4491	-20.11	6.247	-	-	0.1506	-0.4975

2.4 *Comparison with other stress reduction coefficient, r_d, relationships*

Figure 5 shows the proposed r_d relationship (using Eq. 2 for α and β) for magnitudes of 5.5 and 7.5, along with the r_d values predicted by a few commonly used r_d relationships. The Liao & Whitman (1986) relationship is solely a function of depth and was adopted for use in the Youd *et al.* (2001) liquefaction evaluation procedures, which are widely used in practice. Cetin (2000) proposed two variants of an r_d relationship, one being a function of **M**, a_{max}, V_{S12}, and depth (*i.e.*, Cetin with V_{s12}) and the other being a function of **M**, a_{max}, and depth (*i.e.*, Cetin w/o V_{s12}). These relationships were adopted for use in the Cetin *et al.* (2004), Moss *et al.* (2006), and Kayen *et al.* (2013) simplified liquefaction evaluation procedures. The Idriss (1999) r_d relationship is a function of **M** and depth and was adopted for use in the Idriss & Boulanger (2008) and Boulanger & Idriss (2014) liquefaction evaluation procedures.

Relative to the relationship developed herein, all three of the r_d relationships mentioned above yield higher values at shallow depths. Furthermore, the Idriss (1999) and Liao & Whitman (1986) relationships predict higher values of r_d for almost all depths relative to the developed relationship. The Cetin (2000) relationship is less dependent on earthquake magnitude than the proposed relationship and yields values that fall in between the **M** 5.5 and **M** 7.5 curves of the developed relationship; the developed relationship predicts a greater range of r_d values overall. Because the developed

relationship generally predicts lower values of r_d, the use of this relationship will predict smaller values of maximum shear stress (τ_{max}) at depth in a profile for a given value of a_{max}.

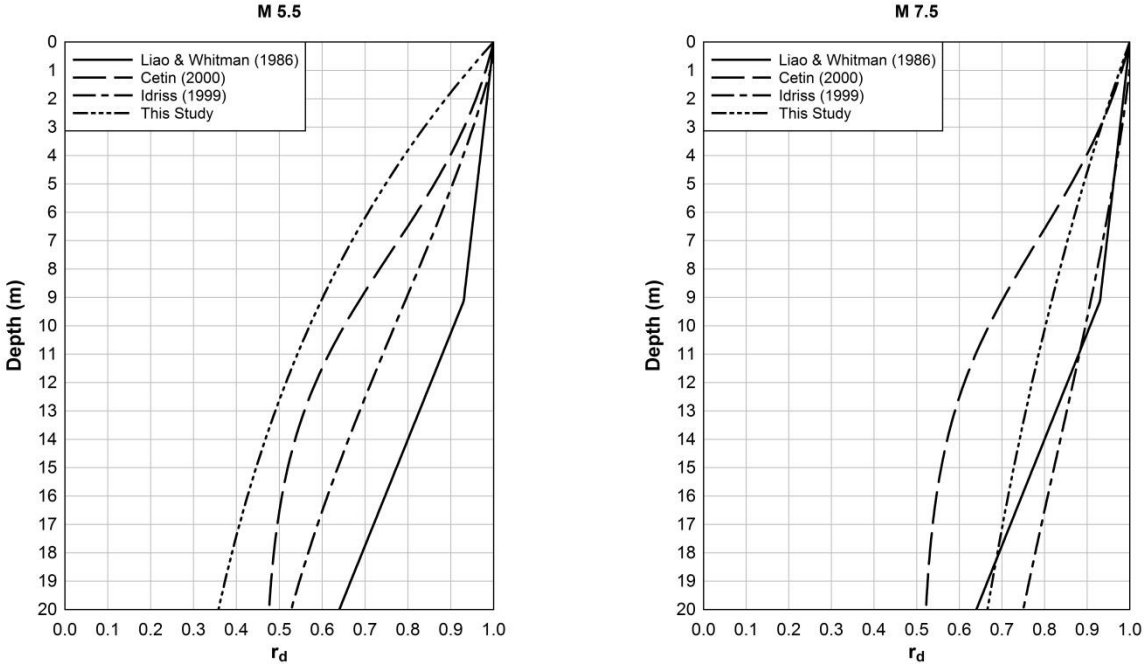

(a) (b)

Figure 5. Comparison of commonly used r_d relationships proposed by Liao & Whitman (1986), Cetin (2000), Idriss (2000), and the one developed herein (Eqs. 1 and 3) for two different earthquake scenarios: (a) **M** 5.5 and a_{max} = 0.1g, and (b) **M** 7.5 and a_{max} = 0.3g. Note: Liao & Whitman (1986) relationship is independent of earthquake magnitude and a_{max}; Idriss (1999) and Eqs. 1 and 3 are only dependent on **M** and depth; and Cetin (2000) is dependent on **M**, a_{max}, and depth.

3. Magnitude Scaling Factors, MSF

Magnitude scaling factors (MSF) account for the influence of the strong motion duration on liquefaction triggering. For historical reasons, MSF is normalized to a magnitude 7.5 earthquake (*i.e.*, MSF = 1 for an **M** 7.5 earthquake). Various proposed MSF relationships are shown in Figure 6. MSF have traditionally been computed as the ratio of the number of equivalent cycles for an **M** 7.5 event to that of a magnitude **M** event, raised to the power *b* (*i.e.*, MSF = $(n_{eq\ M7.5}/n_{eq\ M})^b$). Both the Idriss & Boulanger (2008) and Boulanger & Idriss (2014) used the Seed *et al*. (1975) variant of the Palmgren-Miner (P-M) fatigue theory to compute $n_{eq\ M7.5}$ and $n_{eq\ M}$ from earthquake motions recorded at the surface of soil profiles. Furthermore, they obtained the value of *b* from laboratory test data. *b* is the negative slope of a plot of log(CSR) versus log(N_{liq}), as shown in Figure 7; N_{liq} is the number of cycles required to induce liquefaction in a soil specimen subjected to sinusoidal loading having an amplitude of CSR, typically determined using cyclic triaxial or cyclic simple shear tests.

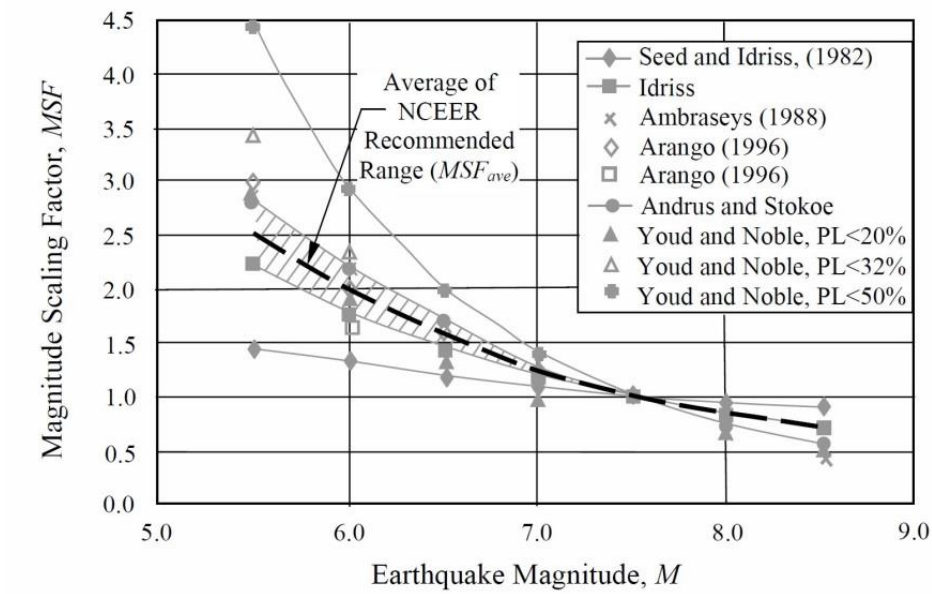

Figure 6. Plot of magnitude scaling factors (MSF) proposed by various investigators. MSF account for the duration of the earthquake shaking, wherein earthquake magnitude is used as a proxy for strong motion duration. For historical reasons, MSF are normalized to **M** 7.5 earthquake (adapted from Youd *et al*., 2001).

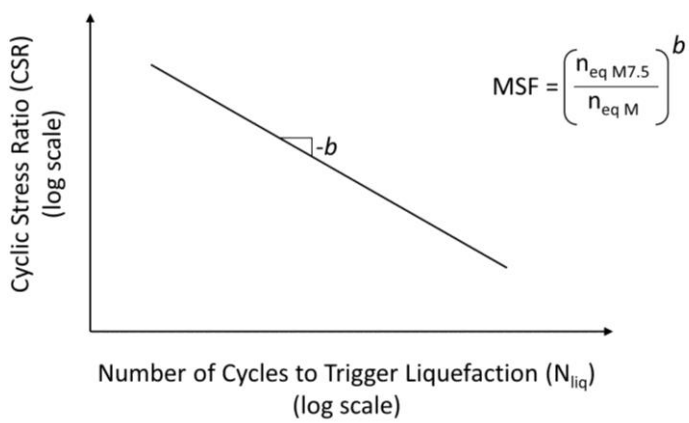

Figure 7. For liquefaction evaluations, the Seed *et al*. (1975) variant of the Palmgren-Miner fatigue theory has most commonly been used to compute the equivalent number of cycles (n_{eq}). Per this approach, the slope of a CSR vs. N_{liq} curve (or *b* value) developed from laboratory tests is used to relate the "damage" induced in a soil sample from a pulse having one amplitude to that having a different amplitude. The *b* value is also used to relate n_{eq} and MSF.

There are several shortcomings inherent to the approach used by Idriss & Boulanger (2008) and Boulanger & Idriss (2014) to compute the number of equivalent cycles and MSF. These include:

- Both the magnitude and uncertainty of n_{eq}, and hence MSF, are assumed to be constant with depth. However, Green & Terri (2005) have shown that n_{eq} can vary with depth in a given profile and more recent analyses (presented subsequently) show that while the median value for n_{eq} computed for a large number of soil profiles and ground motions remains relatively constant with depth, the uncertainty in n_{eq} varies with depth.
- Pulses in the acceleration time history having an amplitude less than $0.3 \cdot a_{max}$ are assumed not to contribute to the inducement of liquefaction, and thus are not considered in the computation of n_{eq}. Using a relative amplitude criterion to exclude pulses is contrary to the known nonlinear response of soil which is governed by the absolute amplitude of the imposed load, among other factors. The use of a relative amplitude exclusion criterion with tectonic earthquake motions may inherently biase the resulting MSF, limiting its validity for use with motions having different characteristics (*e.g.*, motions from induced earthquakes).
- Each of the two horizontal components of ground motion is treated separately, inherently assuming that both components have similar characteristics. However, analysis of recorded motions has shown this is not always the case, particularly in the near fault region (*e.g.*, Green *et al*., 2008; Carter *et al.*, 2014).
- The *b* values used by Boulanger & Idriss (2014) were derived from several laboratory studies performed on various soils and it is uncertain whether all these studies used a consistent definition of liquefaction in interpreting the test data. As a result, the *b* values proposed by Boulanger & Idriss (2014) entail a considerable amount of uncertainty, with the proposed values not being in accord with those inherent to the shear modulus and damping degradation curves used in the equivalent linear site response analyses to develop the r_d correlations (elaborated on subsequently).
- Recent studies have shown that the amplitude and duration of earthquake ground motions are negatively correlated (*e.g*., Bradley, 2011); preliminary models confirm this for Groningen field ground motions, as shown in Figure 8. None of the MSF correlations developed to date have considered this.

Some of the above listed shortcomings will be more significant to the Groningen project than others, but it is difficult to state *a priori* which ones these are. Furthermore, even for tectonic earthquakes the validation of MSF is hindered by the limited magnitude range of case histories in the field liquefaction databases, with the majority of the cases being for events having magnitudes ranging from **M** 6.25 to **M** 7.75 (Figure 9). Specific to the Groningen project, validation of the MSF for small magnitude events is very important, particularly given that published MSF range by a factor of 3 for **M** 5.5 (Figure 6), with this factor increasing if the proposed MSF relations are extrapolated to lower magnitudes.

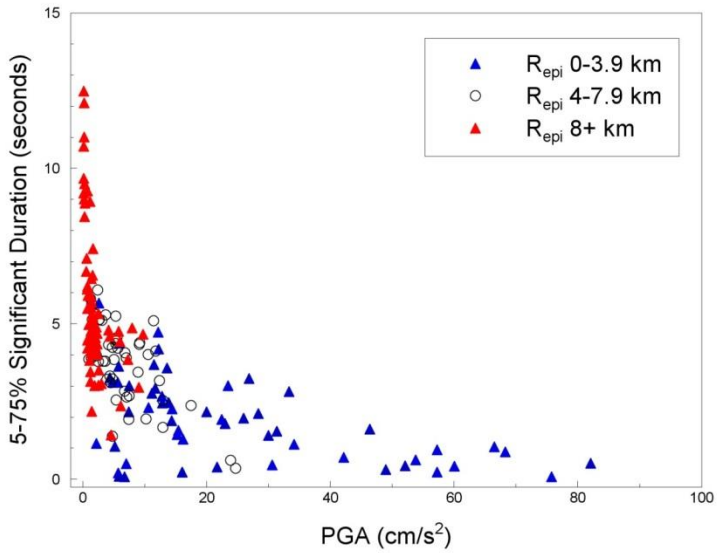

(a)

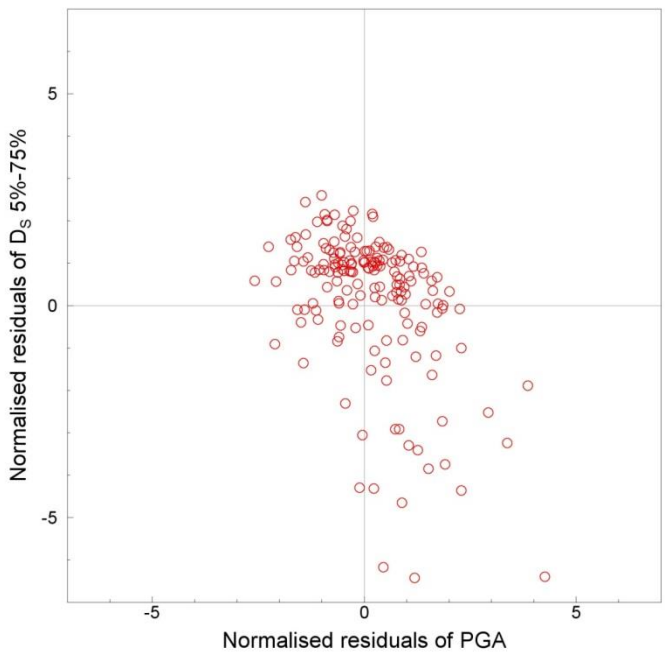

(b)

Figure 8. (a) Individual component pairs of horizontal duration and PGA for the Groningen ground-motion database grouped by epicentral distance of the recording (Note that of the commonly used duration metrics, n_{eq} has the strongest correlation with the 5-75% Significant Duration.); (b) Normalised residuals of PGA and duration for the Groningen database relative to the V1 GMPEs for the prediction of these parameters.

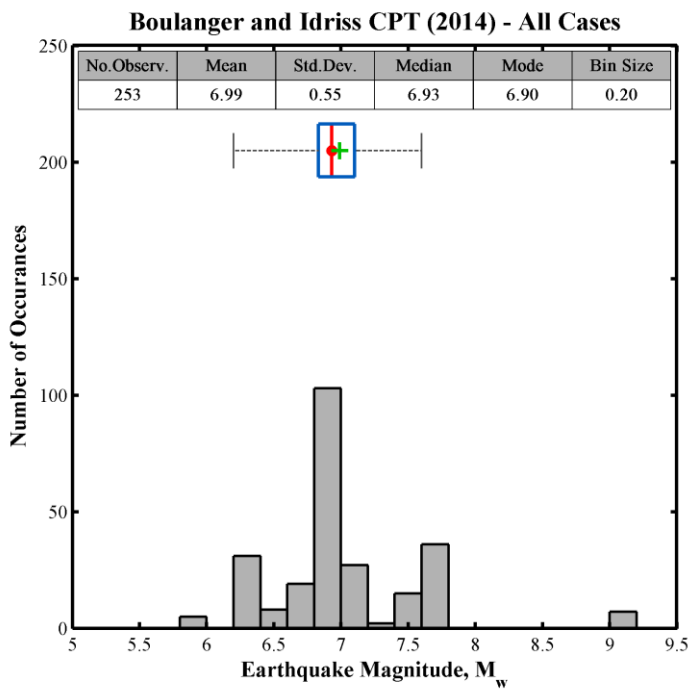

Figure 9. Histogram of earthquake magnitude for the liquefaction case histories in the Boulanger & Idriss (2014) CPT database.

Development of a MSF relationship that overcomes all the shortcomings listed above for the Idriss & Boulanger (2008) and Boulanger & Idriss (2014) relationships was not as straight forward as developing the new r_d relationships (Eqs. 1-3). The reason for this is that there are many more issues with existing MSF than there are for the r_d relationships. As a result, a new approach needed to be used to compute the MSF, as opposed to implementing an existing approach using more comprehensive datasets.

As mentioned previously and shown in Figure 7, MSF are computed from equivalent number of cycles, n_{eq}. Well-established fatigue theories have been proposed for computing n_{eq} for materials having varying phenomenological behaviour; reviews of different approaches for computing n_{eq} are provided in Green & Terri (2005), Hancock & Bommer (2005), and Green & Lee (2006), among others. Developed specifically for use in evaluating liquefaction potential, the approach proposed by Green & Terri (2005) was selected for developing an n_{eq} relationship for the Groningen project. This approach is an alternative implementation of the Palmgren-Miner fatigue theory that better accounts for the non-linear behaviour of the soil than the Seed *et al.* (1975) variant. In this approach, dissipated energy is explicitly used as the damage metric. n_{eq} is determined by equating the energy dissipated in a soil element subjected to an earthquake motion to the energy dissipated in the same soil element subjected to a sinusoidal motion of a given amplitude and a duration of n_{eq}. Dissipated energy was selected as the damage metric because it has been shown to correlate with excess pore pressure generation in saturated cohessionless soil samples subjected to undrained cyclic loading (*e.g.*, Green *et al*., 2000; Polito *et al*., 2008). Furthermore, from a microscopic perspective, the

energy is thought to be predominantly dissipated by the friction between sand grains as they move relative to each other as the soil skeleton breaks down.

Conceptually, the Green & Terri (2005) approach for computing n_{eq} is shown in Figure 10. Stress and strain time histories at various depths in the soil profile are obtained from a site response analysis. By integrating the variation of shear stress over shear strain, the cumulative dissipated energy per unit volume of soil can be computed (*i.e.*, the cumulative area bounded by the stress-strain hysteresis loops). n_{eq} is then determined by dividing the cumulative dissipated energy for the entire earthquake motion by the energy dissipated in one equivalent cycle. For historical reasons, the shear stress amplitude of the equivalent cycle (τ_{avg}) is taken as $0.65 \cdot \tau_{max}$ (Figure 1), and the dissipated energy associated with the equivalent cycle is determined from the constitutive model used in the site response analysis. Additionally, the *b* value that is needed to related n_{eq} to MSF can also be determined from the constitutive model used in the site response analysis, by assuming that the CSR vs. N_{liq} curve shown in Figure 7 is a contour of constant dissipated energy (Figure 11).

In Figure 11, ΔW_{15} is computed using Eq. 6. This equation is based on the assumption that the soil can be modelled as a visco-elastic material, consistent with the assumption inherent to the equivalent linear site response algorithm. For liquefaction evaluations, τ used to compute ΔW_{15} can be determined from the cyclic resistance ratio (CRR) curve from the simplified liquefaction evaluation procedure (*e.g.*, Boulanger & Idriss, 2014). Accordingly, the computed CSR vs. N_{liq} curve corresponds to a soil having a given penetration resistance and confined at an initial effective overburden stress (σ'_{vo}) (*i.e.*, τ = CRR × σ'_{vo}); the small strain shear modulus (G_{max}) for the soil should be consistent with the penetration resistance used to determine CRR.

$$\Delta W_{15} = \frac{2\pi \cdot D_\gamma \cdot \tau^2}{G_{max} \cdot \left(\frac{G}{G_{max}}\right)_\gamma} \times 15 \qquad (6)$$

The damping (D_γ) and the degraded secant shear modulus, $G_{max} \cdot (G/G_{max})_\gamma$, values in Eq. 6 are commensurate with the induced shear strain (γ) in the soil and can be determined iteratively from the shear modulus and damping degradation curves used to model the soil response (*e.g.*, Darendeli and Stokoe, 2001). Once the value of ΔW_{15} is determined, a contour of constant dissipated energy can be computed for different amplitudes of loading by simply computing the number of cycles for the assumed loading amplitude required to dissipate energy equal to ΔW_{15}. *b* is the negative slope of the contour of constant dissipated energy.

The assumption that the CSR vs. N_{liq} curve is a contour of constant dissipated energy inherently implies that the energy dissipated in a given element of soil at the point of liquefaction triggering is unique and independent of the imposed loading characteristics. Several studies have shown that this is a reasonable assumption (*e.g.*, Kokusho & Kaneko, 2014; Polito *et al.*, 2013).

The site response analyses performed to develop the new r_d relationships were also used develop the new n_{eq} relationship herein (*i.e.*, the profiles shown in Figure 3 and the motions listed in Table A1 in Appendix A were used in the equivalent linear site response analyses performed to develop the new n_{eq} relationship). The following sections provide details on the analyses performed and the resulting n_{eq} relationship and MSF.

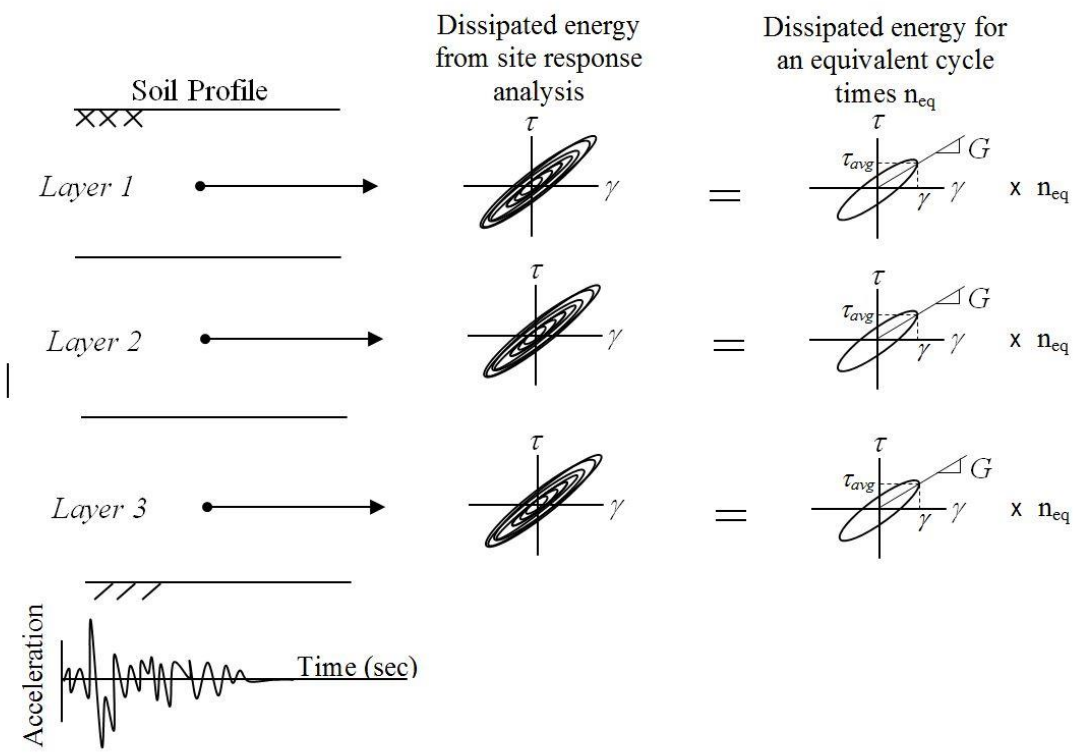

Figure 10. Illustration of the proposed procedure to compute n_{eq}. In this procedure, the dissipated in a layer of soil, as computed from a site response analysis, is equated to the energy dissipated in an equivalent cycle of loading multiplied by n_{eq}.

3.1 *Accounting for multi-directional shaking*

As noted above, one of the shortcomings of the Seed *et al*. (1975) variant of the P-M fatigue theory is the way in which multi-directional shaking is taken into to account. Specifically, each of the two horizontal components of ground motion is treated separately, inherently assuming that both components have similar characteristics. However, analysis of recorded motions has shown this is not always the case, particularly in the near fault region (*e.g.*, Green *et al*., 2008; Carter *et al.*, 2014). In contrast, Green & Terri (2005) accounted for multi-directional shaking by performing separate site response analyses for each horizontal component in a pair of motions, adding the energy dissipated at the respective depths for each component of motion, and setting the amplitude of the equivalent cycle as the 0.65 times the geometric mean

of the maximum shear stresses experienced at a given depth. This approach was adopted for computing the n_{eq} relationship developed herein because it is better able to account for differences in the characteristics in the two horizontal components of motion.

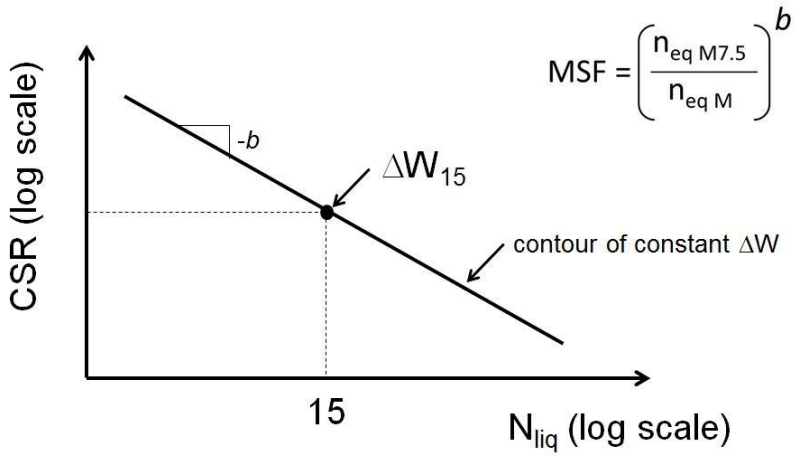

Figure 11. A CSR vs. N_{liq} curve can be computed from shear modulus and damping degradation curves assuming the curve is a contour of constant dissipated energy. ΔW_{15} can be computed using Eq. 6 and the remaining portions of the curve can be computed for different amplitudes of loading by simply computing the number of cycles for the assumed loading amplitude required to dissipated energy equal to ΔW_{15}.

3.2 *n_{eq} correlation*

The selected functional form for the n_{eq} relationship uses a_{max} and M as predictor variables, similar to one of the models proposed by Biondi *et al.* (2004):

$$\ln(n_{eq}) = a_1 + a_2 \ln(a_{max}) + a_3 \boldsymbol{M} + \delta_{event} + \delta_{profile} + \delta_0 \tag{7}$$

where a_{max} is in units of g; a_1-a_3 are regression coefficients; δ_{event} and $\delta_{profile}$ are random effects terms that correspond to an average event residual and the average-profile residuals, respectively; and δ_0 is the residual term. The random effect terms and the residual term are assumed to be zero-mean normally-distributed random variables with standard deviations given by τ_{event}, $\tau_{profile}$, and τ_0 for the event, profile, and residual terms, respectively. Assuming that the random effect terms are uncorrelated, the total standard deviation (σ_{Total}) is given by:

$$\sigma_{Total} = \sqrt{\tau_{event}^2 + \tau_{profile}^2 + \sigma_0^2} \tag{8}$$

The dependency of n_{eq} on a_{max} in Eq. 7 was chosen because of the observed correlation of strong ground motion duration with a_{max}, as illustrated in Figure 8. Also, the functional form of this correlation lends itself for use with simplified liquefaction

evaluation procedures because they require both the magnitude (for MSF) and a_{max} as input variables. It was expected that the shear wave velocity of the layer would be a significant predictor variable, but it was found not to be significant when used in conjunction with a_{max}.

Regressions were performed using the R (R Core Team, 2013) package lme4 (Bates *et al.*, 2014), which implements a mixed effects regression. The use of mixed effects regression avoids potential biases from earthquakes or profile groups that have a relatively large number of data points. Earthquake faulting mechanism was also considered as a random effect, but it was found to be insignificant and, thus, was not use in the final regression analyses. A bootstrapping technique (Efron & Tibshirani, 1994) was employed to obtain the mean and standard deviation of all regression coefficients. The bootstrapping technique was implemented using the following protocol:

1. Ten thousand data points were randomly selected (without replacement) from the dataset of interest.
2. The regression coefficients that best fit the 10,000 data points for the functional form of interest were obtained.
3. Steps 1 and 2 were repeated for 1000 iterations and the regression coefficients for each iteration were recorded.
4. The mean and standard deviation of the distribution of each regression coefficient were calculated.

The mean values and the standard deviations of the regression coefficients for Eq. 7 are given in Table 2. The standard deviation of the regression coefficients is a measure of whether the coefficients are well constrained by the data. The low values of these standard deviations indicate that both the **M** and a_{max} scaling are well constrained by the data.

The standard deviations of the residual components (Eq. 8) are given in Table 3 (in column labelled *Depth-independent model*). Analysis of total residuals indicated that the total standard deviation is depth-dependent, with higher standard deviations near the surface. Since most liquefaction cases occur near the surface, it was deemed important to capture this dependence. Residuals from Eq. 7 were used to constrain a depth-dependent total standard deviation model (σ_{Total}) using a boot-strapping technique. Only the total residuals were fitted in this way. The proposed model is a bilinear relationship given by:

$$\sigma_{Total}(z) = \max\left[\sigma_{surf} - \frac{z}{z_o}\left(\sigma_{surf} - \sigma_{depth}\right),\ \sigma_{depth}\right] \tag{9}$$

where z is depth in meters, σ_{surf} is the standard deviations at the surface, σ_{depth} is the standard deviation at depth, and z_o is the depth at which the standard deviation becomes constant. These parameters are given in Table 3. The depth-dependent standard deviation model is the recommended model to use in applications of Eq. 7.

Table 2. Regression coefficients and standard deviations for n_{eq} correlation (Eq. 7)

a_1	σ_{a_1}	a_2	σ_{a_2}	a_3	σ_{a_3}
0.4605	0.08616	-0.4082	0.009325	0.2332	0.011800

Table 3. Inter-event, intra-event, and total errors for n_{eq} correlation (Eq. 7)

Depth-Independent Model (Eq. 8)				Depth-dependent model (Eq. 9)		
τ_{event}	$\tau_{profile}$	σ_0	σ_{Total}	σ_{surf}	σ_{depth}	z_o (m)
0.4051	0.1856	0.3851	0.5889	0.5399	0.4626	26.4

3.3 *b-value used to compute MSF*

As discussed above, MSF have traditionally been computed as the ratio of the number of equivalent cycles for a **M** 7.5 event to that of a magnitude **M** event, raised to the power *b* (*i.e.*, MSF = $(n_{eq\ M7.5}/n_{eq\ M})^b$), as shown in Figure 7. Also, traditionally the value of *b* has been obtained from laboratory test data (*i.e.*, *b* is the negative slope of a plot of log(CSR) vs. log(N_{liq}), also shown in Figure 7). The *b* values used by Boulanger & Idriss (2014) were derived from several laboratory studies performed on various soils and are expressed as a function of soil density (*i.e.*, *b* increases as soil density increases). This is shown in Figure 12, with soil density expressed in terms of normalized CPT tip resistance (q_{c1Ncs}).

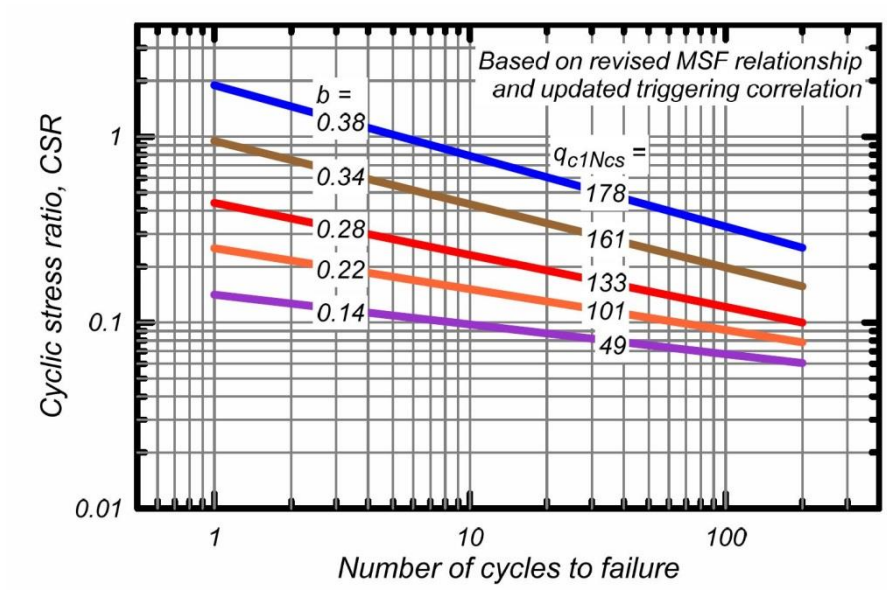

Figure 12. Plot of CSR vs. N_{liq} curves proposed by Boulanger & Idriss (2014) to compute MSF. The slope (-*b*) of the curves is a function of the density of the soil, expressed in terms of normalized CPT tip resistance (q_{c1Ncs}). These curves were developed from several laboratory studies performed on various soils. (From Boulanger & Idriss, 2014)

Expressing *b* as a function of soil density had a significant impact on Boulanger & Idriss' n_{eq} and MSF. Note that the Seed *et al*. (1975) variant of the P-M fatigue theory, which was used by Boulanger & Idriss (2014), requires *b* to compute n_{eq}, as well as *b* being

required to compute MSF from n_{eq}. This combined influence resulted in the MSF proposed by Boulanger & Idriss (2014) being strongly dependent on soil density, as shown in Figure 13. Of particular note are the MSF shown in this figure for loose soils (*i.e.*, MSF curve for $(N_1)_{60cs}$ = 10 blows/30 cm, q_{c1Ncs} = 84 atm). Because this MSF curve is relatively flat, it is implied that the durational effects of the motions for an **M** 4.5 event, for example, are almost as deleterious as those for an **M** 9 event from a liquefaction triggering perspective. Although the amplitude of the earthquake motions also needs to be considered in evaluating liquefaction potential, it would be expected that far more cases of liquefaction would have been observed following small magnitude events if the MSF for loose soils are accurately represented by the curve shown in Figure 13.

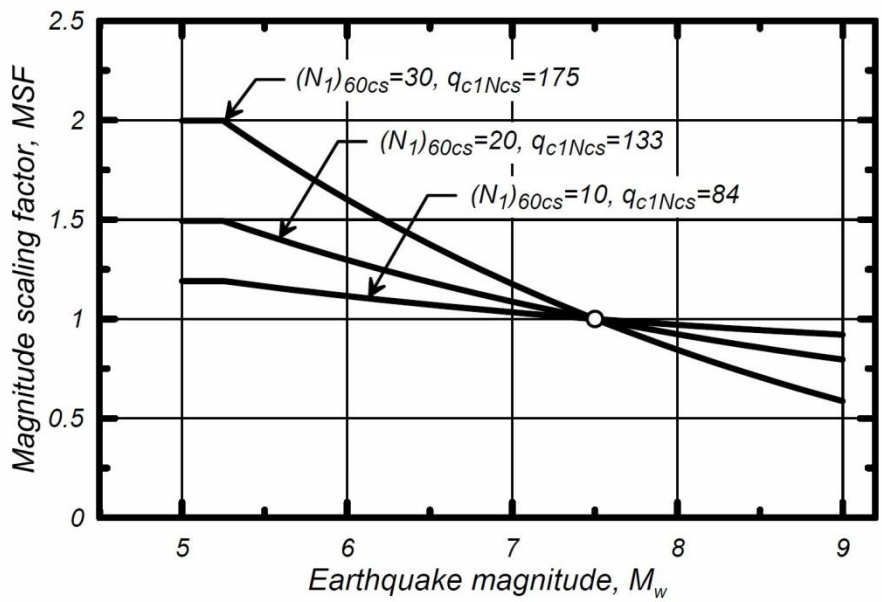

Figure 13. MSF proposed by Boulanger & Idriss (2014). These MSF are a function of soil density, which is expressed in terms of normalized SPT blow count ($(N_1)_{60cs}$) and normalized CPT tip resistance (q_{c1Ncs}). (From Boulanger & Idriss, 2014)

Green & Terri (2005) discuss several significant shortcomings in the Seed *et al*. (1975) variant of the P-M fatigue theory for computing n_{eq} for liquefaction evaluations. As a result and as discussed above, the alternative implementation of the P-M fatigue theory proposed by Green & Terri (2005) was used to compute n_{eq} herein. Although *b* is not explicitly specified in this alternative approach to compute n_{eq}, inherently a *b* value is associated the shear modulus and damping degradation curves used in the equivalent linear site response analyses to compute n_{eq}. The degradation curves proposed Darendeli & Stokoe (2001) were used in these analyses. Following the procedure outlined above in relation to Figure 11, *b* values were computed using the Darendeli & Stokoe (2001) curves for a range of effective confining stresses and soil densities, with the resulting values ranging from 0.33 to 0.35. However, *b* = 0.34 for the vast majority of the confining stress-density combinations considered and was thus used herein to

compute MSF from n_{eq} (discussed subsequently). Additionally, *b* = 0.34 is also consistent with laboratory curves developed from high-quality undisturbed samples obtained by freezing (Yoshimi *et al.*, 1984).

There are a few possible reasons for the dichotomy in studies showing *b* being dependent versus independent of soil density (*e.g.*, *b* = 0.34 for a range of densities versus *b* varying with density as shown in Figure 12). First, Boulanger & Idriss (2014) derived the *b* values shown in Figure 12 from several laboratory studies performed on various soils. Inherent differences in soil characteristics, sample preparation methods, testing apparatuses, and definitions of liquefaction can all influence laboratory determined *b* values. For tests performed as part of a given study, there is no ubiquitous trend of increasing *b* with soil density, as illustrated by the data plotted in Figure 14. (Note that the curvature in the CSR vs. N_{liq} curves in Figure 14 is a result of CSR being plotted on arithmetic scale, and not logarithmic scale.). The data shown in this figure is from DeAlba *et al.* (1976) and is from large-scale (2.3 m x 1.1 m x 0.1 m) simple shear tests performed on Monterey No. 0 sand, which is a uniform sand with a mean grain diameter of about 0.36 mm and a uniformity coefficient of approximately 1.5. As may be observed in this figure, the *b* value corresponding to a relative density (Dr) of 54% is 0.23, while *b* = 0.21 for Dr equal to 68% and 82%, not in accord to the trend shown in Figure 12. The *b* value for CSR vs. N_{liq} curve for Dr = 90% is equal to 0.25, larger than for the lower relative densities. However, this curve is based on only two points, and only one of these points in reported in DeAlba *et al.* (1976); Boulanger & Idriss (2014) and the references cited therein do not mention how the second point for Dr = 90% was determined. In line with the test results shown in Figure 14, Figure 15 shows data from bench-scale cyclic simple shear tests (~64 mm dia. by ~24 mm high samples) also performed on Monterey No. 0 sand (C. Baxter 2016, *unpublished data*). As shown in this figure, the CSR vs. N_{liq} curve for the lower range of relative densities is higher than that for the higher relative densities, again not in accord with the trend shown in Figure 12. Note that the ranges of the densities for tests shown in Figure 15 are well within those for samples of a given soil prepared following the same procedure; many studies choose to state the “nominal” density of the samples, which is often taken as the average of the range of actual sample densities. Other studies also show that the trend of increasing *b* with increasing density is not ubiquitous for a given soil.

Another possible reason for the dichotomy in studies regarding the dependency of *b* on soil density is related to how liquefaction is defined in loose versus dense laboratory samples. For loose samples, liquefaction is often defined as residual excess pore pressure ratio (r_u) equal to 1. However, for dense samples often r_u never reaches 1 due to the dilative tendency of denser soil and alternative definitions of liquefaction are often used (*e.g.*, 5% double amplitude axial strain in cyclic triaxial tests; 7.5% double amplitude shear strain in cyclic simple shear tests). This inconsistency could result in differences in *b* values.

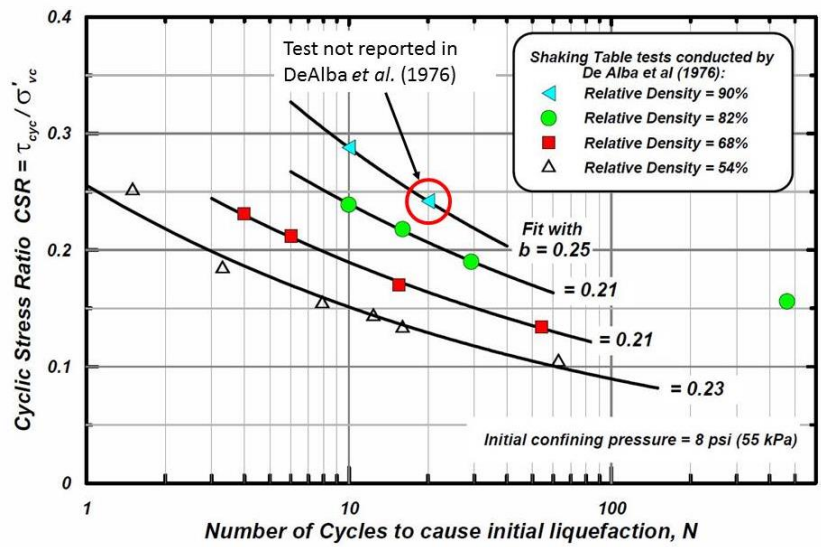

Figure 14. CSR vs. N_{liq} curves from large-scale cyclic simple shear tests performed on Monterey No. 0. All but one point plotted are reported in DeAlba *et al.* (1976); it is uncertain how the additional point corresponding to a relative density of 90% was determined by Boulanger & Idriss (2014). (From Boulanger & Idriss, 2014)

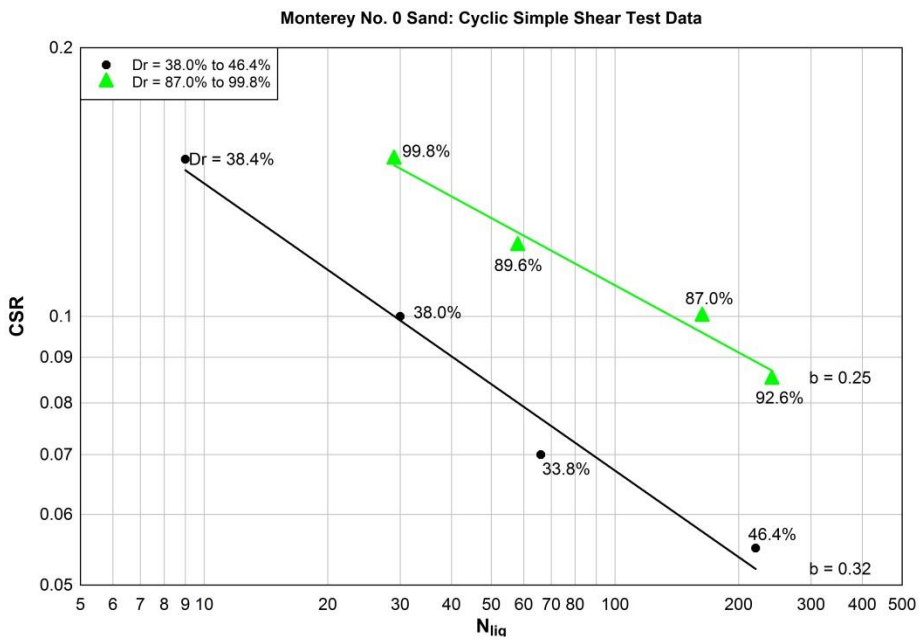

Figure 15. CSR vs. N_{liq} curves from small-scale cyclic simple shear tests performed on Monterey No. 0. (C. Baxter 2016, Univ. Rhode Island, *unpublished data*)

3.4 *Magnitude Scaling Factors, MSF*

As discussed above, MSF account for the durational effects of strong ground shaking on liquefaction triggering. For historical reasons, MSF is normalized to an **M** 7.5

earthquake. MSF were developed herein using the new n_{eq} relationship (Eq. 7), per approach shown in Figure 11, *i.e.*:

$$MSF = \left(\frac{n_{eq\ M7.5}}{n_{eq\ M}}\right)^{b} \tag{10}$$

As mentioned previously, $n_{eq\ M7.5}$ is the equivalent number of cycles for an **M** 7.5 earthquake (which is the normalization parameter), $n_{eq\ M}$ is the equivalent number of cycles for an event having a magnitude **M**, and *b* is the negative slope of the log(CSR) vs. log(N_{liq}) curve. To compute $n_{eq\ M7.5}$ using Eq. 7, **M** is set to 7.5 and a value for a_{max} needs to be assumed (*i.e.*, $a_{max7.5}$). $a_{max7.5}$ was determined by computing the average a_{max} for the case histories in the Boulanger & Idriss (2014) SPT and CPT liquefaction case history databases ranging in magnitude from 7.4 to 7.6. The average a_{max} for the 116 case histories that fell within this magnitude range was ~0.35 g. Using this value for $a_{max7.5}$, $n_{eq\ M7.5}$ was computed to be ~14. This value is similar to that determined by Seed *et al.* (1975), *i.e.*, $n_{eq\ M7.5}$ = 15. However, the value reported by Seed *et al.* (1975) represents the average for two horizontal components of motion, while the value computed herein represents the combined influence of both components of motion. As a result, the value computed herein is approximately half of that computed by Seed *et al.* (1975). This difference is due both to the significantly larger, more robust ground motion database used herein to compute $n_{eq\ M7.5}$, compared to that used by Seed *et al.* (1975), and to the differences in the approaches used to compute n_{eq}. However, both of these differences also influence the denominator in Eq. 10, which minimizes their influence on the resulting MSF.

Using $n_{eq\ M7.5}$ = 14 and *b* = 0.34, the new MSF relationship is:

$$MSF = \left(\frac{14}{n_{eq}(M, a_{max})}\right)^{0.34} \leq 2.02 \tag{11}$$

where the denominator is determined from Eq. 7. The upper limit on the MSF (*i.e.*, 2.02) corresponds to a scenario where the earthquake motions consist of a single shear stress pulse in one of the horizontal components of motion. A plot of Eq. 11 is shown in Figure 16 for magnitudes ranging from 5.0 to 8.5 and a_{max} ranging from 0.1 to 1.0 g.

A first order approximation for the standard deviation of the natural log of the MSF is:

$$\sigma_{\ln(MSF)} = b \cdot \sqrt{\sigma^2_{\ln(n_{eq\ M7.5})} + \sigma^2_{\ln(n_{eq\ M})} - 2 \cdot \rho \cdot \sigma_{\ln(n_{eq\ M7.5})}\sigma_{\ln(n_{eq\ M})}} \tag{12}$$

where $\sigma_{\ln(n_{eq\ M7.5})}$ and $\sigma_{\ln(n_{eq\ M})}$ are the standard deviations of the ln($n_{eq\ M7.5}$) and ln(n_{eqM}), respectively, and ρ is the correlation coefficient of the residuals of ln($n_{eq\ M7.5}$) and ln($n_{eq\ M}$). However, because $n_{eq\ M7.5}$ is simply a normalization parameter for a reference scenario, $\sigma_{\ln(n_{eq\ M7.5})}$ = 0 and the correlation between the residuals of

$\ln(n_{eqM7.5})$ and $\ln(n_{eq\ M})$ is also zero (*i.e.*, $\rho = 0$). Accordingly, the standard deviation of the natural logarithm of the MSF reduces to:

$$\sigma_{\ln(MSF)} = b \cdot \sigma_{\ln(n_{eq\ M})} \tag{13}$$

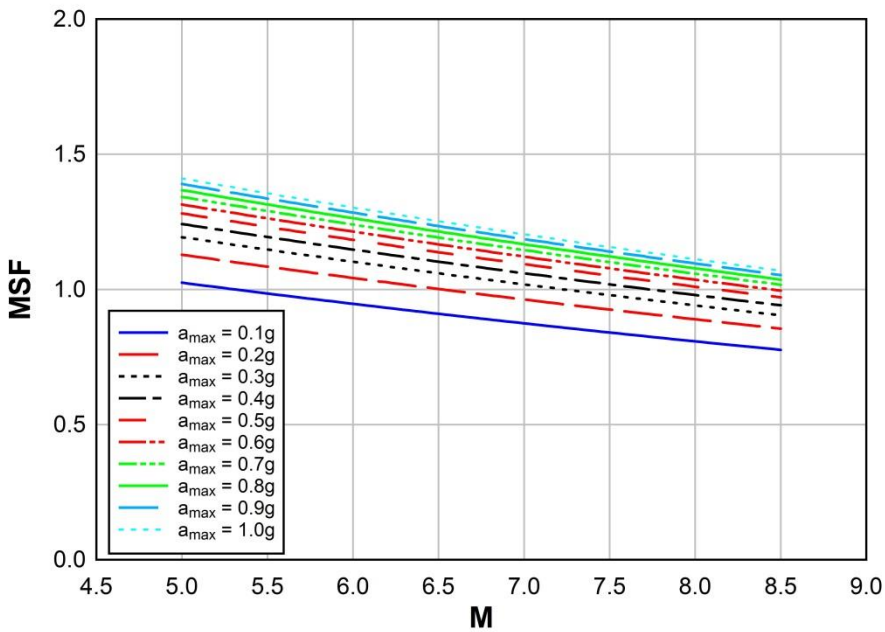

Figure 16. MSF developed herein. For a given magnitude earthquake, MSF increases as a_{max} increases.

Figure 17 shows a comparison of the MSF developed herein with those proposed by Idriss & Boulanger (2008) and Boulanger & Idriss (2014), where the latter is shown for q_{c1Ncs} = 84, 133, and 175 atm. As may be observed from this figure, for a given value of a_{max} the MSF developed herein has about the same dependency on magnitude as the MSF proposed by Boulanger & Idriss (2014) for q_{c1Ncs} = 84 atm (*i.e.*, loose to medium dense sand) However, the difference between the two is that the former is a function of a_{max}, with MSF for a given magnitude increasing as a_{max} increases.

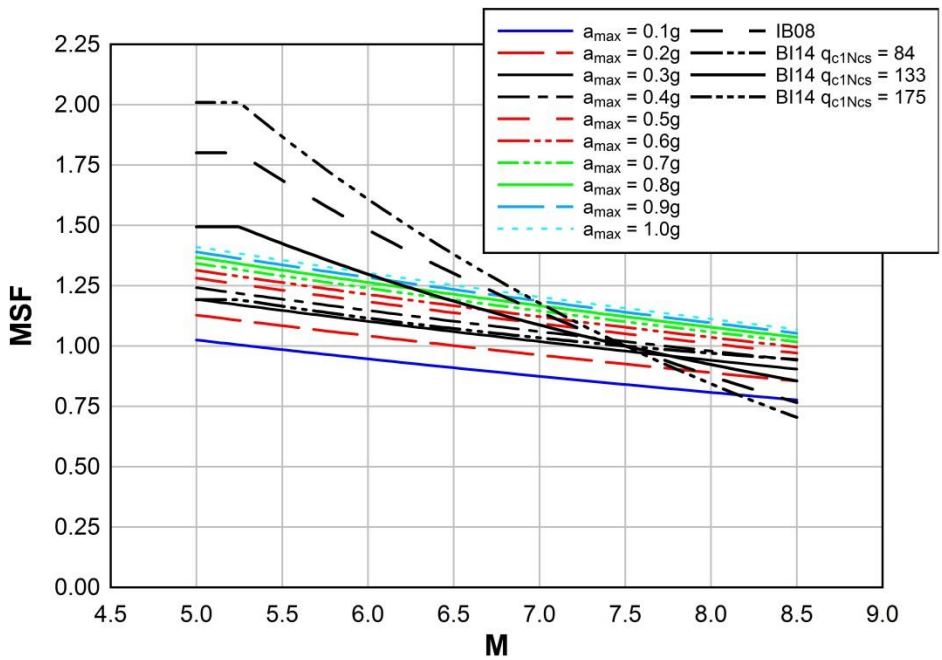

Figure 17. Comparison of the MSF developed herein and those proposed by Idriss & Boulanger (2008) and Boulanger & Idriss (2014).

To compare the efficacy of the MSF developed herein versus that proposed by Boulanger & Idriss (2014), each is used within the Boulanger & Idriss (2014) simplified liquefaction evaluation framework to analyse the case histories in the CPT liquefaction case history database compiled by Boulanger & Idriss (2014). All other adjustment, normalization, and correction factors proposed by Boulanger & Idriss (2014) were used, to include r_d. The results of this effort are plotted in Figure 18, where CSR* is the CSR (Figure 1) divided by MSF and an overburden correction factor (K_σ). Also shown in these plots are the deterministic cyclic resistance ratio (CRR) curves for **M** 7.5 (*i.e.*, $CRR_{7.5}$) with the curve plotted in Figure 18a being a slight modification of the one proposed by Boulanger & Idriss (2014) and plotted in Figure 18b. As may be observed form these plots, the MSF developed herein caused a slight shifting of some of the points, which is the reason for the slight modification applied to $CRR_{7.5}$ curve shown in Figure 18a. With this modification, the $CRR_{7.5}$ curves shown in Figure 18a and 18b are equally efficacious in separating the respective liquefaction/marginal liquefaction and no liquefaction cases.

The same conclusion regarding the relative efficacy of the two MSF was obtained from the analysis of several thousand case studies from the 2010-2011 Canterbury, New Zealand, earthquake sequence, wherein the simplified liquefaction evaluation procedures were used in conjunction with the LPI framework (Iwasaki *et al.*, 1978) to evaluate the predicted versus observed severity of surficial liquefaction manifestations. Following the approach used by Green *et al.* (2015), Maurer *et al*. (2015a), and Maurer *et al*. (2015b), Receiver Operator Characteristic (ROC) analyses were performed on the computed data. The results from these analyses are shown in Figure 19, where the curves shown in this figure are referred to as ROC curves (Fawcett, 2005). The area

under each of the ROC curves is a measure of the MSFs' efficacy; the larger the area under the curve (AUC) the more efficacious the MSF. As may be observed from the ROC curves, the MSF developed herein and those proposed by Boulanger & Idriss (2014) are essentially equally efficacious in separating no surficial liquefaction manifestations from marginal, moderate, or severe manifestations (Figure 19a) and in separating no surficial liquefaction manifestations from moderate or severe manifestations (Figure 19b).

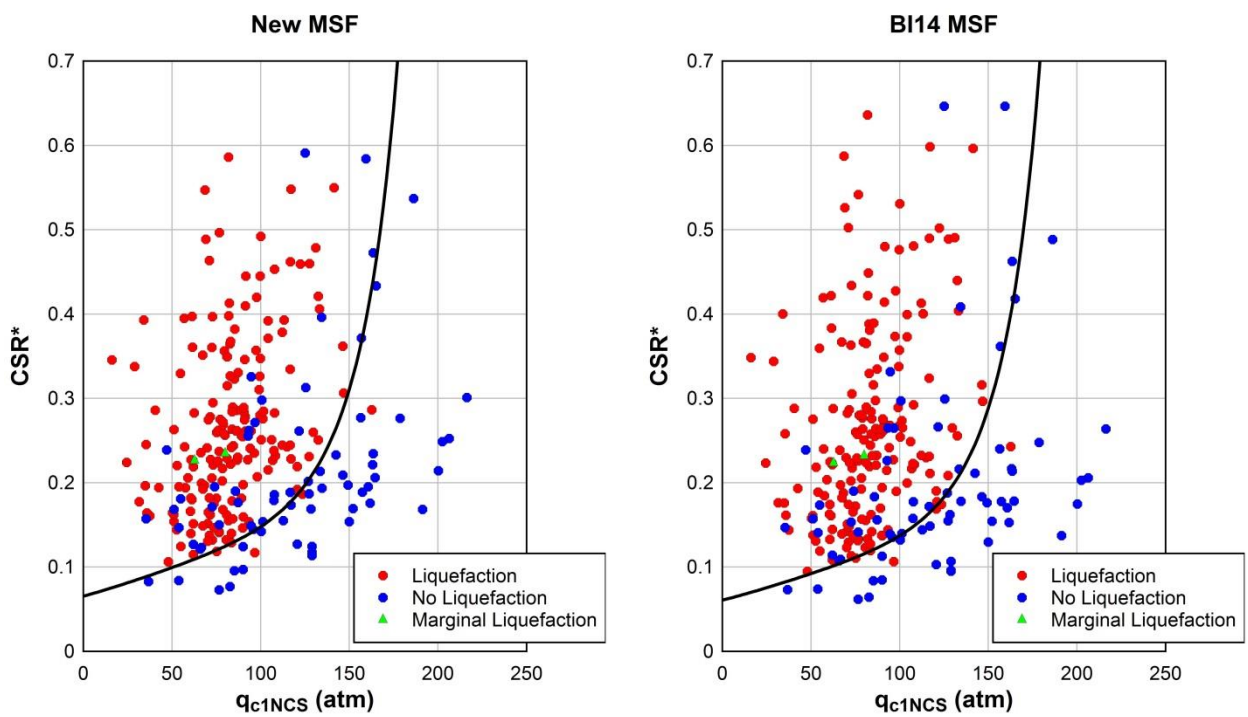

(a) (b)

Figure 18. Reanalysis of CPT liquefaction case histories from the Boulanger & Idriss (2014) database using: (a) MSF developed herein; and (b) MSF proposed by Boulanger & Idriss (2014). For both sets of analyses, the MSF were used within the Boulanger & Idriss (2014) simplified liquefaction evaluation framework.

Although the results presented in Figures 18 and 19 show that the MSF developed herein and those proposed by Boulanger & Idriss (2014) have the same efficacy in predicting liquefaction triggering and severity of surficial liquefaction manifestations, the cases analysed in Figure 18 represent a fairly limited range in earthquake magnitude (Figure 9), and the cases analysed from the CES sequence had magnitudes of 6.2 and 7.0 (Green *et al.*, 2015). To assess the efficacy of the MSFs for lower magnitude events that are more relevant to the Groningen region, data from the Garner Valley Downhole Array (GVDA) and the Wildlife Liquefaction Array (WLA) are analysed. Both of these arrays are located in southern California and were part of the US National Science Foundation (NSF) George E. Brown, Jr. Network for Earthquake Engineering Simulation (NEES) and are run by the University of California at Santa Barbra (*i.e.*, NEES@UCSB).

Since the ending of NSF funding for all NEES facilities in September 2014, the operation and maintenance of the GVDA and WLA is being funded by the US Nuclear Regulatory Commission (NRC). The subsurface conditions at the GVDA and the WLA are very well characterized and the sites are permanently instrumented with surface and borehole arrays of accelerometers and pore pressure transducers designed to record strong ground motions and excess pore pressure generation (Steidl & Seale, 2010).

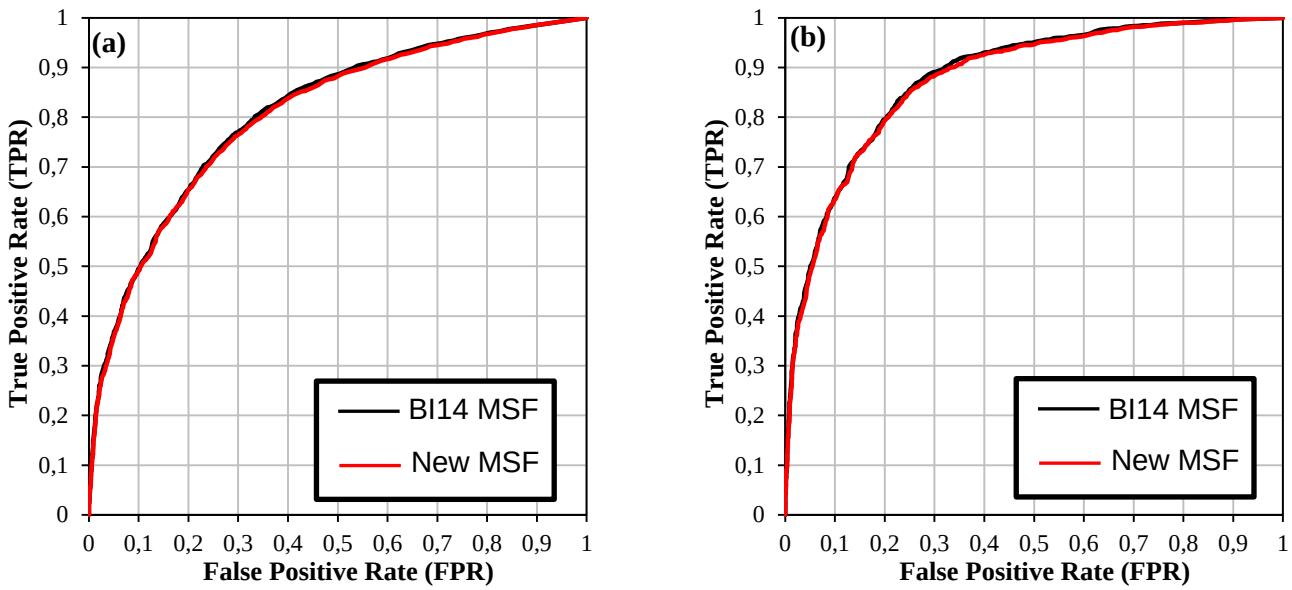

Figure 19. Receiver Operator Characteristic (ROC) curves used to assess the relative efficacy of the MSF developed herein versus those proposed by Boulanger & Idriss (2014). (a) Efficiency in separating no surficial liquefaction manifestations from marginal, moderate, or severe manifestations; (b) Efficiency in separating no surficial liquefaction manifestations from moderate or severe manifestations (marginal removed from dataset).

Of specific interest to assess the efficacy of the MSF are data from events that caused shaking at the sites that was intense enough to generate excess pore pressures, but not intense enough to induce liquefaction (*i.e.*, $0 < r_u < 1$). Additionally, the events had to be sufficiently isolated in time from other events so that proper interpretation of both the ground motions and the recorded pore pressures could be made. Example motions and pore pressure recordings from such an event are shown in Figure 20, which were recorded at the WLA during an **M** 4.9 earthquake that was part of the August 2012 Brawley Earthquake Swarm (Hauksson *et al.*, 2013). Central to computing MSF from the measured excess pore pressures are a $CRR_{7.5}$ curve (e.g., Figure 18), a CSR vs. N_{liq} curve (*e.g.*, Figure 11), an n_{eq} model (*e.g.*, Eq. 7), and an excess pore pressure generation model that relates r_u and cycle ratio (*i.e.*, the number of loading cycles of a given amplitude divided by the number of cycles having the same amplitude that is required to induce liquefaction) (*e.g.*, Booker *et al.*, 1976; Polito *et al.,* 2008). From these, correlations between r_u and factor of safety against liquefaction (FS_{liq}) can be derived for the specific conditions of interest (*e.g.*, soil density, initial vertical effective confining stress, and CSR). Examples of such correlations are shown in Figure 21 for

the top of the liquefiable layer (GL-2.54) at the WLA (Figure 20) and for a liquefiable layer at a depth of 6.2 m (GL-6.2) at the GVDA. Note that differences in the CSR vs. N_{liq} curves and the n_{eq} models inherent to the MSF developed herein and those proposed by Boulanger & Idriss (2014) result in different r_u vs. FS_{liq} correlations.

Using an r_u vs. FS_{liq} correlation computed for the stratum of interest, the maximum residual r_u measured during an earthquake is used to determine the FS_{liq} for the ground motions experienced at the site, and MSF is computed using Eq. 14:

$$MSF = \frac{FS \cdot CSR}{CRR_{7.5} \cdot K_{\sigma}} \tag{14}$$

where CSR is for the earthquake that caused the excess pore pressure generation, and $CRR_{7.5}$ and K_{σ} are for stratum in which the excess pore pressures were measured.

Figure 21 shows a comparison of the predicted and back-calculated MSF for the four events listed in Table 4. The comparison is made for both the MSF developed herein and for those proposed by Boulanger & Idriss (2014). Note that differences in the r_u vs. FS_{liq} correlations for the two MSF relationships result in different back-calculated MSF. Although predicted and back-calculated MSF do not exactly match for either MSF relationship, the back-calculated values are more in accord those predicted using the MSF developed herein than with Boulanger & Idriss (2014).

Table 4. Earthquakes resulting in excess pore pressure generation at WLA and GVDA and used to back-calculate MSF

Site	Date	**M**	a_{max} (g)	Depth (m)	$N_{1,60cs}$ (blows/30 cm)	r_u
WLA	1 Sept 2005	3.65	0.056	2.54	18.9	0.0125
WLA	26 Aug 2012	4.61	0.292	2.54	18.9	0.58
WLA	27 Aug 2012	4.90	0.327	2.54	18.9	0.63
GVDA	7 July 2010	5.43	0.065	6.2	18	0.075

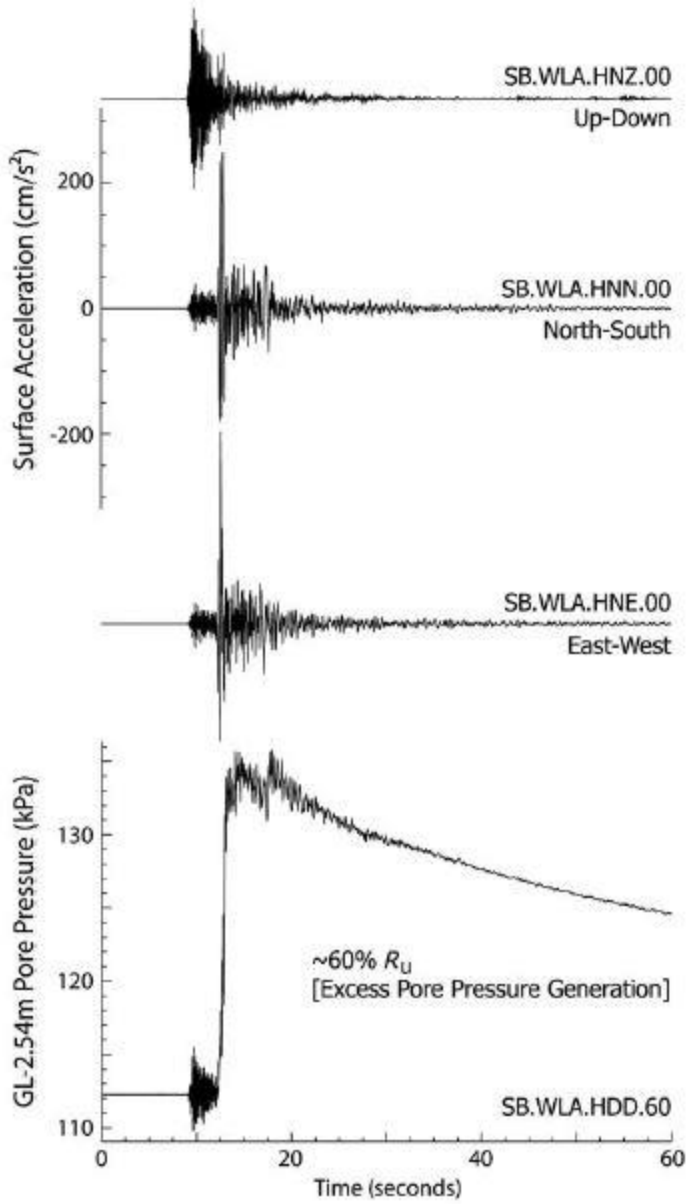

Figure 20. Ground-motion and pore pressure response from the 04:41 UTC 27 August 2012 **M** 4.9 earthquake. The top three traces are the acceleration time histories with peak ground motions over 0.3 g. The bottom trace is the resulting pore pressure response at 2.54 m depth (GL-2.54) with an excess pore pressure ratio (r_u) of 63% at the top of the liquefiable layer. (From Hauksson *et al*., 2013)

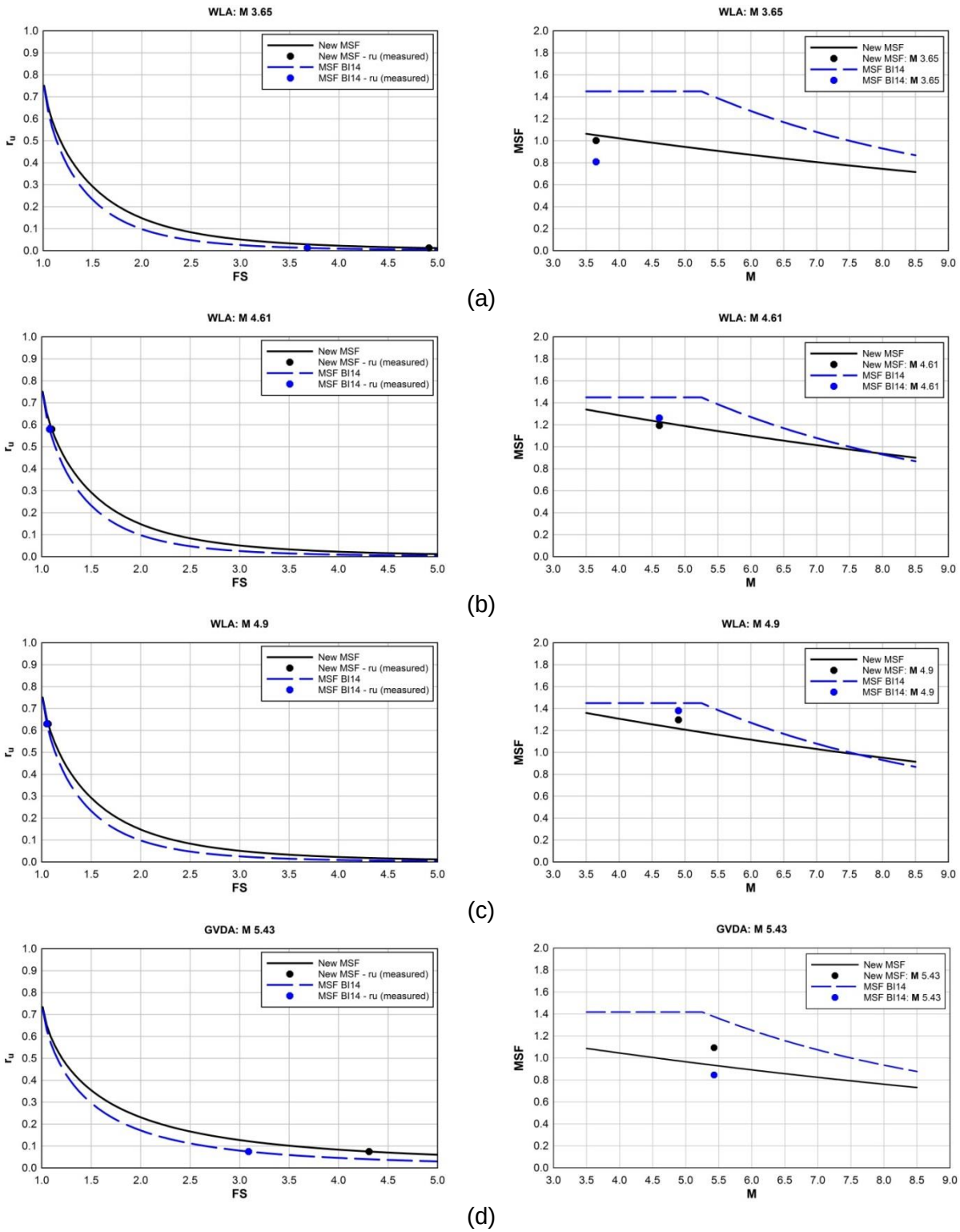

Figure 21. Comparison of predicted and back-calculated MSF from seismically induced excess pore water pressure from the WLA and GVDA. The back-calculations were performed using correlation derived from the MSF developed herein and from the MSF proposed by Boulanger & Idriss (2014). (a) WLA: 1 September 2005, **M** 3.65, (b) WLA: 26 August 2012, **M** 4.61, (c) WLA: 27 August 2012, **M** 4.9, and (d) GVDA: 7 July 2010, **M** 5.43.

4. Combined Influence of New r_d and MSF Relationships

4.1 *Efficacy of the new r_d and MSF relationships in combination*

The comparisons shown in Figures 18 and 19 were made to assess the relative efficacy of the MSF developed herein versus that proposed by Boulanger & Idriss (2014) and did not involve the use of the new r_d relationship. To assess the relative efficacy of the combination of the MSF and r_d relationships developed herein versus those proposed by Boulanger & Idriss (2014), the analyses were repeated using both of the new relationships. Figure 22 shows a comparison of the analysis of the case histories in the CPT liquefaction case history database compiled by Boulanger & Idriss (2014), using the MSF and r_d relationships developed herein within the Boulanger & Idriss (2014) simplified liquefaction evaluation framework (Figure 22a) and Boulanger & Idriss (2014) procedure as they proposed it (Figure 22b). Also shown in these plots is the deterministic $CRR_{7.5}$ curve proposed by Boulanger & Idriss (2014), without any modification applied to either Figure 22a or 22b. As may be observed form these plots, the MSF and r_d relationships developed herein caused a slight shifting of some of the points, but the $CRR_{7.5}$ proposed by Boulanger & Idriss (2014) is equally efficacious in separating the respective liquefaction/marginal liquefaction and no liquefaction cases.

The case studies from the 2010-2011 Canterbury, New Zealand, earthquake sequence were also re-analysed using the MSF and r_d relationships developed herein. As before, the analyses were performed in conjunction with the LPI framework to evaluate the predicted versus observed severity of surficial liquefaction manifestations and ROC analyses were performed on the results (Figure 23). As may be observed from Figure 23, the AUC corresponding to the Boulanger & Idriss (2014) MSF and r_d relationships are slightly larger than those for the curve corresponding to the MSF and r_d relationships developed herein. However, the differences in the AUCs are very slight and efficacy of the two sets of MSF and r_d relationships is considered to be the same for the cases analysed.

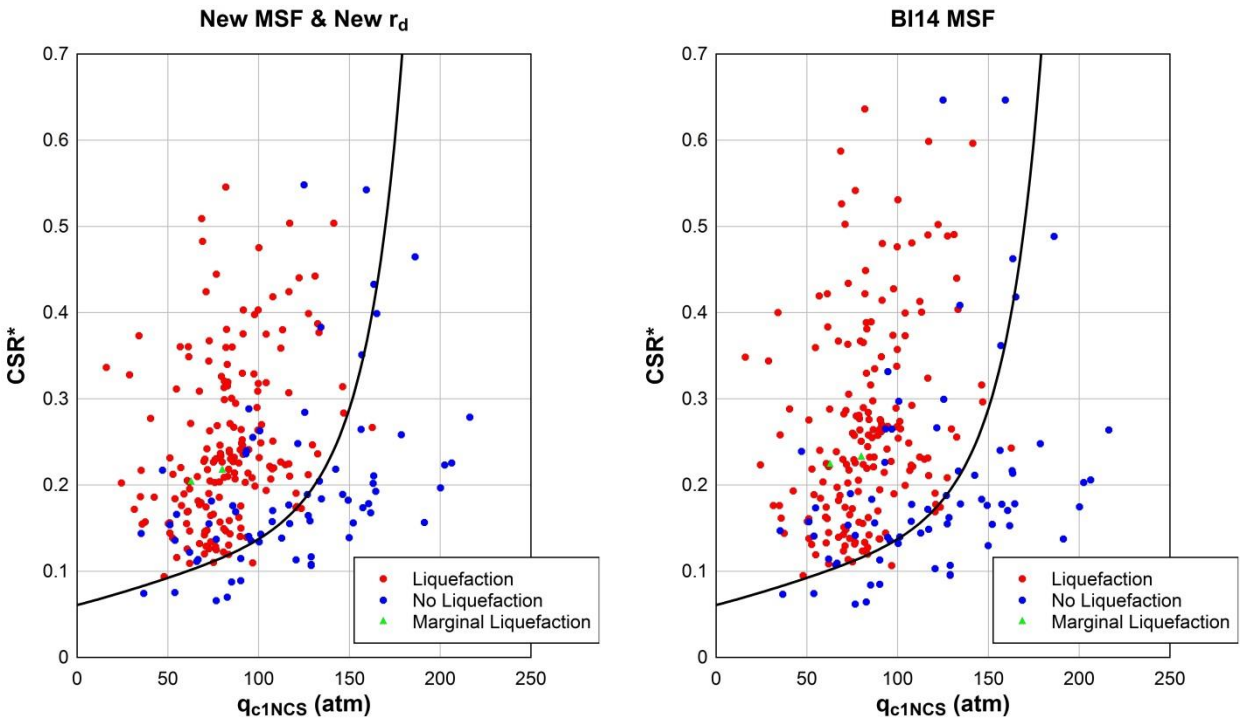

(a) (b)

Figure 22. Reanalysis of CPT liquefaction case histories from the Boulanger & Idriss (2014) database using: (a) MSF and r_d developed herein; and (b) MSF proposed by Boulanger & Idriss (2014). For both sets of analyses, the MSF and r_d were used within the Boulanger & Idriss (2014) simplified liquefaction evaluation framework.

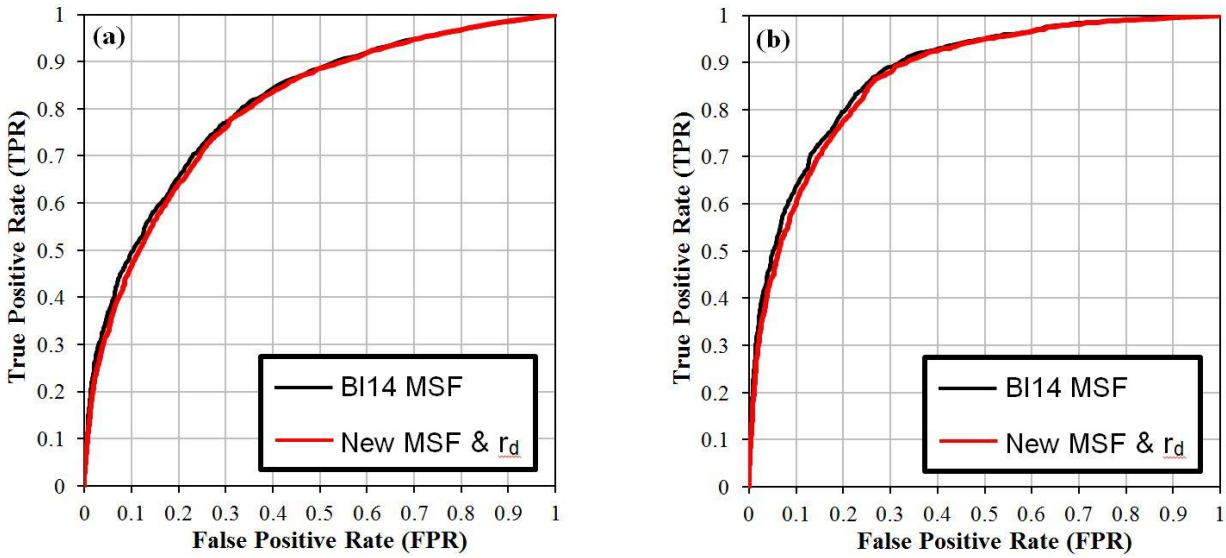

Figure 23. Receiver Operator Characteristic (ROC) curves used to assess the relative efficacy of the MSF and r_d relationships developed herein versus those proposed by Boulanger & Idriss (2014). (a) Efficiency in separating no surficial liquefaction manifestations from marginal, moderate, or severe manifestations; (b) Efficiency in separating no surficial liquefaction manifestations from moderate or severe manifestations (marginal removed from dataset).

To further evaluate the relative efficacy of the two sets of the MSF and r_d relationships, 280 case histories from worldwide earthquakes were analysed using the LPI-ROC framework (*e.g.*, Green *et al.*, 2015; Maurer *et al.*, 2015a; Maurer *et al.*, 2015b). The starting point for identifying case histories to be analysed was the database used by Boulanger and Idriss (2014) to develop their CPT liquefaction evaluation procedure (*i.e.*, the case histories corresponding to the data plotted in Figure 22). However, of the 253 cases listed in Boulanger and Idriss (2014) approximately 30 were not used herein because either the log of measured tip resistance and/or sleeve friction for the case history could not be obtained. For the majority of remaining cases, only hard copies of the CPT sounding logs could be obtained, which were digitized for use herein. Additional case histories reported in literature were also collected for analysis herein, most notably the cases from the 20 May 2012, **M** 6.1 Emilia, Italy, earthquake (Papathanassiou *et al*., 2015). However, the collected worldwide case histories were only categorized as either "liquefaction" or "no liquefaction" because descriptions of the surficial liquefaction manifestations needed to refine the severity categorization were not readily obtainable. The results from the analysis of the worldwide case histories are shown in Figure 24. As may be observed from this figure, the AUC corresponding to the new MSF and r_d relationships developed herein is slightly larger than that for the curve corresponding to Boulanger & Idriss (2014) (*i.e.*, 0.779 vs. 0.778). However, as with the AUC for the 2010-2011 Canterbury, New Zealand, earthquake data (Figure 23), the difference in the AUCs is very slight and efficacy of the two sets of MSF and r_d relationships is considered to be the same for these cases.

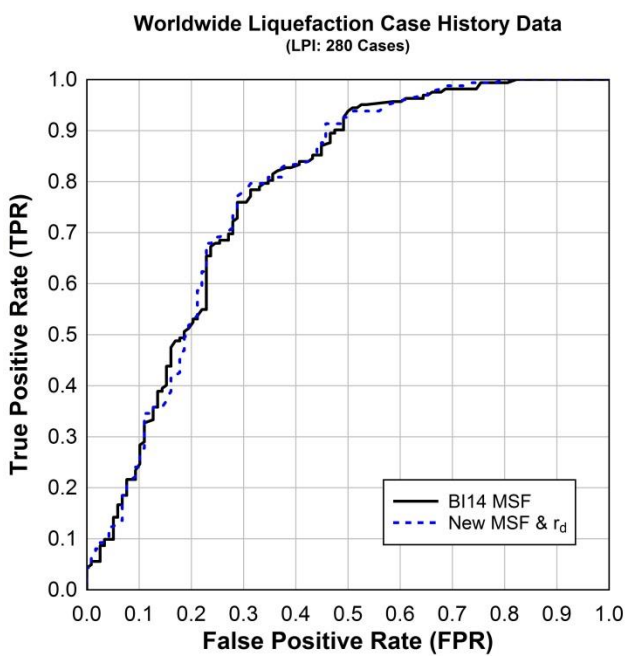

Figure 24. Receiver Operator Characteristic (ROC) curves for worldwide case history data categorized as either "liquefaction" or "no liquefaction." The areas under the ROC curves can be used to assess the relative efficacy of the MSF and r_d relationships developed herein versus those proposed by Boulanger & Idriss (2014) in separating "liquefaction" versus "no liquefaction" cases.

Other ongoing work that can potentially provide insights relative efficacy of the new MSF and r_d relationships developed herein versus those proposed by Boulanger & Idriss (2014) is data that is currently be collected and analysed from the **M** 5.7 Valentine's Day earthquake that impacted Christchurch, New Zealand, on 14 February 2016. The epicentre for the event was ~8 km offshore of Christchurch (to the east in Pegasus Bay). The significance of this event is that intensity of shaking across Christchurch ranged from low to moderate, potentially allowing the threshold level of shaking required to induce liquefaction to be constrained. Comparisons of field observations with preliminary maps of predicted surficial liquefaction severity computed using Boulanger & Idriss (2014) liquefaction evaluation procedure in conjunction with the LPI framework show mixed results (*i.e.*, predictions that are and are not in accord with field observations). Severity maps developed using the new MSF and r_d relationships proposed herein are still being computed, and it is unknown at this time whether these maps will be in better accord with field observations than the Boulanger & Idriss (2014) based maps.

4.2 *Impact of new r_d and MSF relationships on liquefaction predictions*

As shown in Figure 22, the deterministic $CRR_{7.5}$ curves developed from the case histories analysed using the new MSF and r_d relationships proposed herein and those proposed by Boulanger & Idriss (2014) are identical. Additionally, the comparisons presented above using the 2010-2011 Canterbury, New Zealand, earthquake sequence liquefaction data and the worldwide case history data show the relative efficacy of the MSF and r_d relationships proposed herein versus those proposed by Boulanger & Idriss (2014) are essentially identical for the range of scenarios considered. However, this does not imply that the two sets of MSF and r_d relationships will yield the same predictions for the occurrence of liquefaction for all scenarios of interest.

To evaluate when the two sets of MSF and r_d relationships yield different predictions, the ratio of the factors of safety against liquefaction, FS_{liq}, computed using the new MSF and r_d relationships proposed herein and those proposed by Boulanger & Idriss (2014) were computed for a range of scenarios: earthquake magnitudes ranging from **M** 4 to **M** 8; peak ground accelerations (a_{max}) ranging from 0.01 to 1 g; normalized CPT tip resistances (q_{c1Ncs}) equal to 50, 100, and 150 atm; and critical depths (z_{liq}) equal to 1, 2.5, 5, 10, and 15 m. For all scenarios, the depth to the ground water table (z_{gwt}) was assumed to be 1 m. The computed FS_{liq} ratios are shown in Figure 25 for q_{c1Ncs} = 50 atm (loose), Figure 26 for q_{c1Ncs} = 100 atm (medium dense), and Figure 27 q_{c1Ncs} = 150 atm (dense) sandy soil. The trends shown in these figures are the result of the interplay between the influence of the r_d relationships and the MSF relationships.

For q_{c1Ncs} = 50 atm (loose sandy soil, Figure 25), there is a monotonic increase in the FS_{liq} ratio (*i.e.*, $FS_{unbiased}/FS_{BI14}$, where $FS_{unbiased}$ is the FS_{liq} computed using the new MSF and r_d relationship proposed herein and FS_{BI14} is the FS_{liq} computed using the MSF and r_d relationship proposed by Boulanger & Idriss (2014)) for increasing a_{max} and z_{liq}, and a monotonic decrease in FS_{liq} ratio for increasing earthquake magnitude. For

the majority of the scenarios (*i.e.*, $a_{max} \geq 0.2$ g), the FS_{liq} computed using the Boulanger & Idriss (2014) over predicts liquefaction susceptibility, relative to when the new MSF and r_d relationships proposed herein are used. This trend becomes more pronounced as a_{max} increases (as a result of the MSF relationship proposed herein being a function of a_{max}) and even more so as the depth to liquefaction increases (as a result of the r_d relationship proposed herein reflecting a less rigid response of the soil profile than the relationship proposed by Boulanger & Idriss (2014)). For larger magnitude events and lower a_{max} (*i.e.*, $a_{max} < 0.1$ g), the FS_{liq} ratio is less than one. However, for cases where a_{max} is small, the maximum shear strain induced in the soil by the earthquake shaking should be computed and compared to the threshold strain required to generate residual excess pore water pressures (Dobry *et al.,* 1982). If the maximum induced shear strain at a given depth in a soil profile does not exceed a threshold value (*i.e.,* $\gamma \sim 0.01\%$), residual excess pore pressures will not be generated, and thus, liquefaction will not be induced regardless of the FS_{liq} computed using a stress-based liquefaction evaluation procedure.

As the density of the soil increases (*e.g.*, q_{c1Ncs} = 100 atm – medium dense sandy soil, Figure 26; q_{c1Ncs} = 100 atm – dense sandy soil, Figure 27), the influence of the Boulanger & Idriss (2014) MSF's dependency on soil density has a more pronounced effect, resulting in a reduction in the FS_{liq} ratios relative to those for looser soils. However, for many of the scenarios where the FS_{liq} ratio is less than one, the density of the soil is such that liquefaction susceptibility is low and the FS_{liq} computed with either set of MSF and r_d relationships is much greater than 1.0.

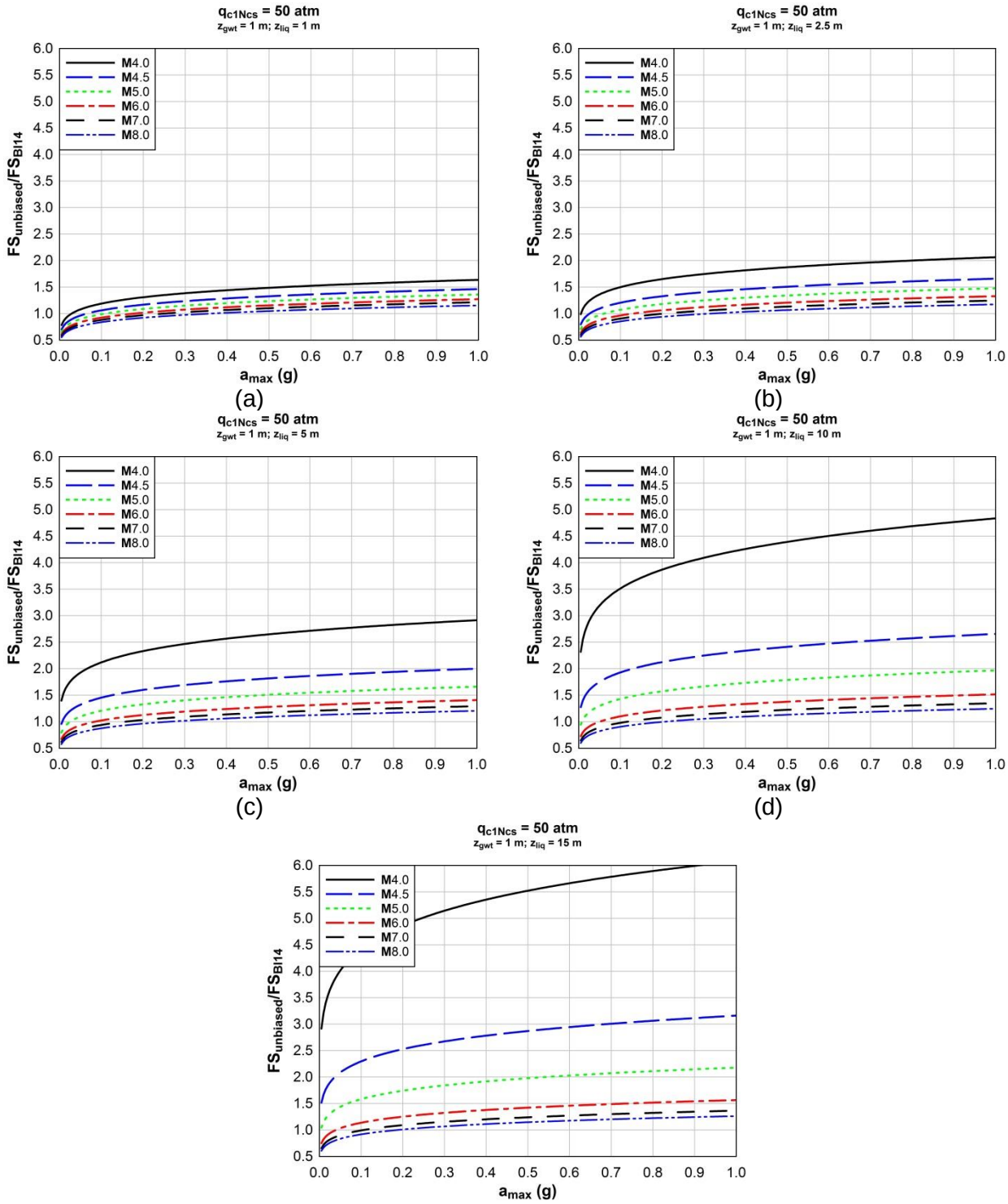

Figure 25. Ratio of the FS_{liq} computed using the MSF and r_d relationships proposed herein to the ones proposed by Boulanger & Idriss (2014) for soil having q_{c1Ncs} = 50 atm for a range of earthquake scenarios and depth to liquefaction: (a) z_{liq} = 1 m, (b) z_{liq} = 2.5 m, (c) z_{liq} = 5 m, (d) z_{liq} = 10 m, and (e) z_{liq} = 15 m.

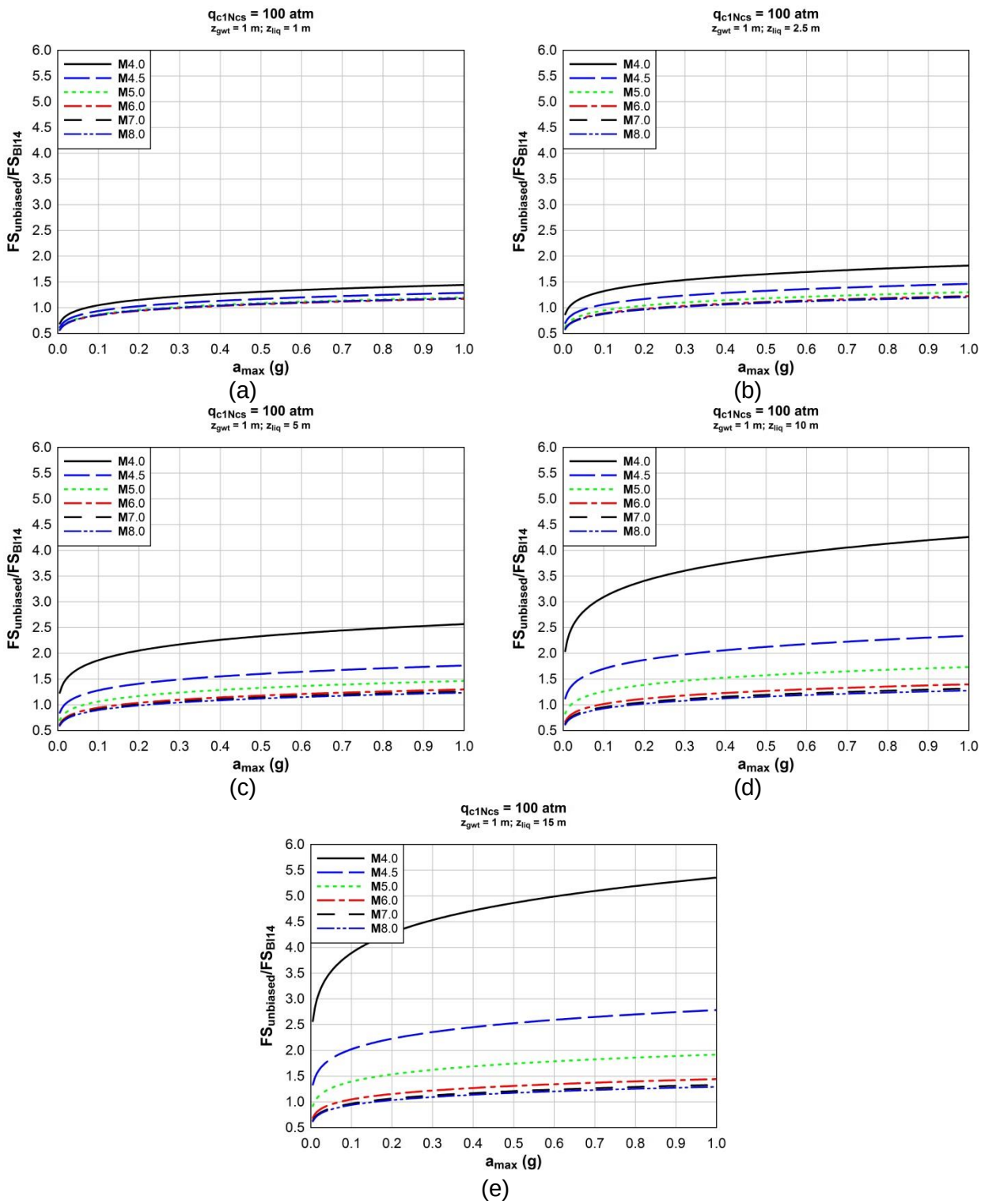

Figure 26. Ratio of the FS_{liq} computed using the MSF and r_d relationships proposed herein to the ones proposed by Boulanger & Idriss (2014) for soil having q_{c1Ncs} = 100 atm for a range of earthquake scenarios and depth to liquefaction: (a) z_{liq} = 1 m, (b) z_{liq} = 2.5 m, (c) z_{liq} = 5 m, (d) z_{liq} = 10 m, and (e) z_{liq} = 15 m.

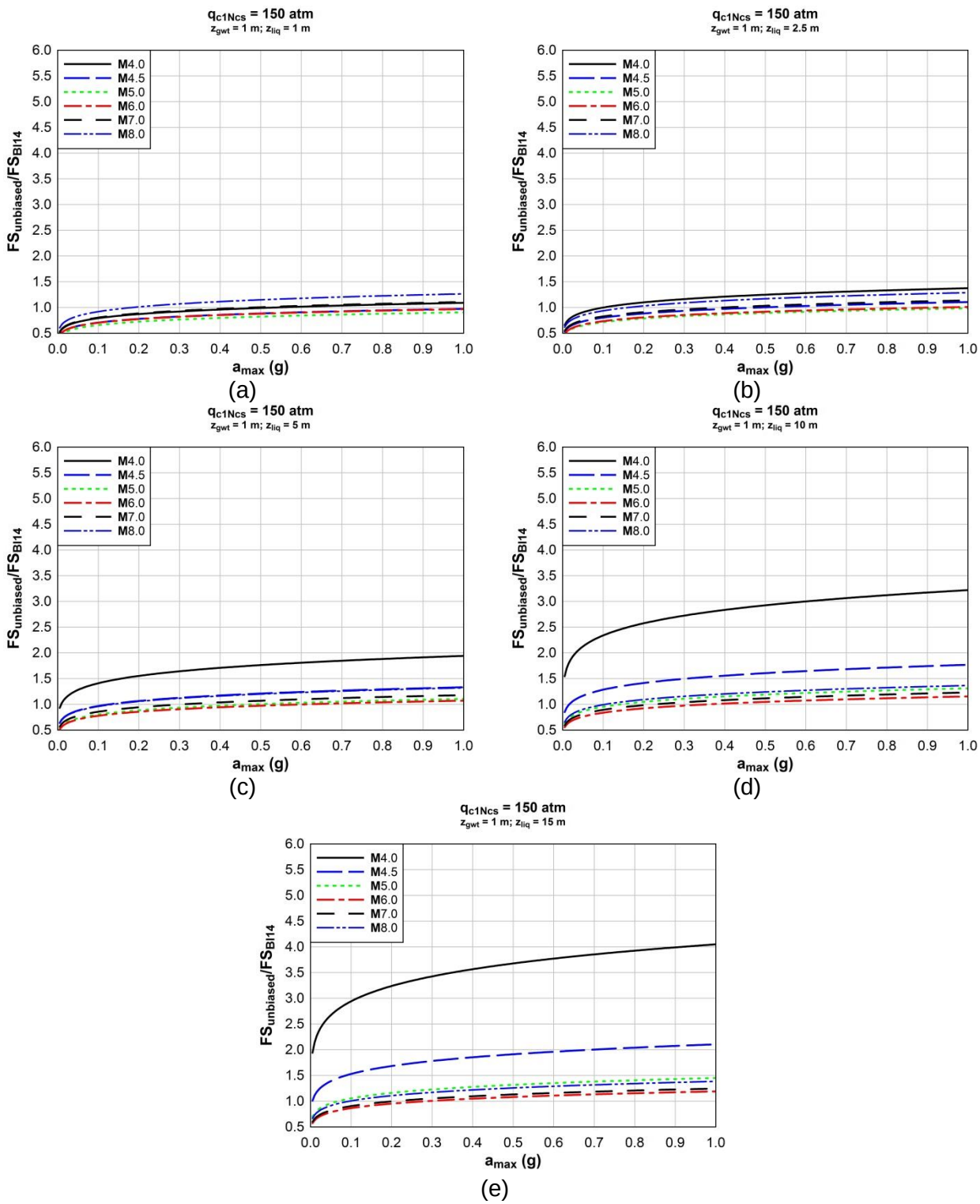

Figure 27. Ratio of the FS_{liq} computed using the MSF and r_d relationships proposed herein to the ones proposed by Boulanger & Idriss (2014) for soil having q_{c1Ncs} = 150 atm for a range of earthquake scenarios and depth to liquefaction: (a) z_{liq} = 1 m, (b) z_{liq} = 2.5 m, (c) z_{liq} = 5 m, (d) z_{liq} = 10 m, and (e) z_{liq} = 15 m.

5. Unbiased Probabilistic CRR Relationship

The CRR curves shown in Figure 22 are deterministic and can be used to compute FS_{liq}. However, to incorporate the liquefaction hazard predictions into a risk framework, probabilistic forms of the CRR curves are needed, where the results from the liquefaction hazard evaluation are quantified in terms of the probability of liquefaction being triggered, P(liq), as opposed to the FS_{liq}. Several investigators have proposed CPT-based probabilistic CRR curves in the past, to include Juang *et al.* (2002), Moss *et al.* (2006), and Boulanger & Idriss (2014). However, the details of how each of these studies developed their CRR relationships differ to some degree and the uncertainty accounted for by the resulting relationships also differ (*e.g.*, total uncertainty vs. model uncertainty). These differences make a direct comparison of the proposed curves difficult and, more importantly, influence how the curves are used and the results interpreted.

To develop the probabilistic CRR curves herein, the approach outlined in Boulanger & Idriss (2014) was generally followed. In this approach, most of the liquefaction triggering analysis components are based on experimental and theoretical considerations, as opposed to including them as unknown fitting parameters in the regression analysis. This adds constraints to the regression analysis which is necessary because the ranges in the influencing variables (*e.g.*, penetration resistance, fines content, effective confining stress, earthquake magnitude, a_{max}, *etc.*) represented by the case histories used in the regression analyses are relatively limited. The shortcoming of not constraining the regression analysis is illustrated by the probabilistic CRR relationship proposed by Moss *et al.* (2006) which is relatively insensitive to earthquake magnitude, despite the influence of ground motion duration on liquefaction triggering being well known. Following the Boulanger & Idriss (2014) approach, the regressions were performed on data quantified in terms of CSR*, q_{c1Ncs}, and liquefaction response (*e.g.*, "liquefaction" or "no liquefaction"), with uncertainties of each taken into account. The only difference in the dataset regressed by Boulanger & Idriss (2014) and that regressed herein are the CSR* values, which result from the different MSF and r_d relationships used.

Boulanger & Idriss (2014) used the following limit state function, which was also adopted herein:

$$g\left(\hat{Q},\hat{S},C_o,\varepsilon_Q,\varepsilon_{\ln(R)},\varepsilon_{\ln(S)}\right) = exp\left[\frac{\hat{Q}+\varepsilon_Q}{113}+\left(\frac{\hat{Q}+\varepsilon_Q}{1000}\right)^2-\left(\frac{\hat{Q}+\varepsilon_Q}{140}\right)^3+\left(\frac{\hat{Q}+\varepsilon_Q}{137}\right)^4-C_o\right]+ \varepsilon_{\ln(R)}-\ln(S)-\varepsilon_{\ln(S)} \quad (15)$$

where $\hat{Q}$ is the estimated value of q_{c1Ncs}, $\hat{S}$ is the estimated value of CSR*, R is the estimated value for $CRR_{7.5}$, and C_o is a curve fitting parameter. The error terms ε_Q, $\varepsilon_{ln(R)}$, $\varepsilon_{ln(S)}$ are assumed to have means of zero and standard deviations of σ_Q, $\sigma_{ln(R)}$, $\sigma_{ln(S)}$, respectively. If the values of Q, S, σ_Q, and $\sigma_{ln(S)}$ are specified, the only remaining curve fitting parameters are C_o and $\sigma_{ln(R)}$. The functional form of Eq. 15 is based on the

Boulanger & Idriss (2014) deterministic liquefaction curve (Figure 22), for which C_o = 2.8 and the error terms are not considered.

The likelihood function that is used herein, again adopted from Boulanger & Idriss (2014), is:

$$L = \prod_{Liq\ Cases} min\left(P_{min}, \Phi\left[-\frac{\hat{g}(\hat{Q},\hat{S},C_o)}{\sigma_T}\right]^{\omega_{liq}}\right) \times \prod_{No\ Liq\ Cases} min\left(P_{min}, \Phi\left[-\frac{\hat{g}(\hat{Q},\hat{S},C_o)}{\sigma_T}\right]^{\omega_{no\ liq}}\right) \quad (16)$$

where $\Phi[\cdot]$ is the standard cumulative normal probability function; P_{min} is the minimum allowable probability (which can be used to minimizes the influence of outlying case histories on the determination of the regression parameters); ω_{liq} and $\omega_{no\ liq}$ are weighting factors that account for disproportionate numbers of "liquefaction" and "no liquefaction" case histories; and σ_T is the total standard deviation, approximated by:

$$\sigma_T = \sqrt{\left(\frac{1}{113} + \frac{2\hat{Q}}{1000^2} - \frac{3\hat{Q}^2}{140^3} + \frac{4\hat{Q}^3}{137^4}\right)\sigma_Q^2 + \sigma_{\ln(R)}^2 + \sigma_{\ln(S)}^2} \quad (17)$$

The resulting probabilistic relationship for $CRR_{7.5}$ is given as:

$$CRR_{7.5} = exp\left[\frac{q_{c1Ncs}}{113} + \left(\frac{q_{c1Ncs}}{1000}\right)^2 - \left(\frac{q_{c1Ncs}}{140}\right)^3 + \left(\frac{q_{c1Ncs}}{137}\right)^4 - C_o + \sigma_T \cdot \Phi^{-1}(P_L)\right] \quad (18)$$

where C_o = 2.632, σ_T = 0.468, Φ^{-1} is the inverse of the standard cumulative normal distribution, and P_L is the probability of liquefaction. For the regression analysis, P_{min} = 0 was assumed, which means that outlying case histories were given full weight. A plot of the equation is shown in Figure 28 (green lines). For use in forward liquefaction evaluation analyses, the conditional probability of liquefaction for known values of CSR* and q_{c1Ncs} can be computed by:

$$P_L(q_{c1Ncs}, CSR^*) = \Phi\left[-\frac{\frac{q_{c1Ncs}}{113} + \left(\frac{q_{c1Ncs}}{1000}\right)^2 - \left(\frac{q_{c1Ncs}}{140}\right)^3 + \left(\frac{q_{c1Ncs}}{137}\right)^4 - 2.632 - ln(CSR^*)}{\sigma_T}\right] \quad (19)$$

While the functional forms of Eqs. 18 and 19 are the same as those proposed by Boulanger & Idriss (2014), the uncertainties accounted for in these equations differ. Specifically, Eqs. 18 and 19 account for the total uncertainty (which includes the uncertainty in q_{c1Ncs}, CSR*, and $CRR_{7.5}$, where the latter is referred to as model uncertainty). Accordingly, in using Eq. 19 in a forward analysis to compute the probability of liquefaction, median values for q_{c1Ncs} and CSR* should be used because the uncertainties in q_{c1Ncs} and CSR* are already accounted for in σ_T.

In contrast to Eqs. 18 and 19, the probabilistic relationship for $CRR_{7.5}$ recommended by Boulanger & Idriss (2014) only accounts for model uncertainty (Figure 28, black lines), which was quantified using judgement (*i.e.*, the case history data was not able to constrain $\sigma_{ln(R)}$, so Boulanger & Idriss (2014) used judgement to determine this value). As result, the use of the Boulanger & Idriss (2014) equations in a forward analysis to compute the probability of liquefaction requires the explicit specification of uncertainties in q_{c1Ncs} and CSR* by the user. Due to the differences in the probabilities that are account for by the two probabilistic $CRR_{7.5}$ relationships, a direct comparison of the relationships proposed herein and by Boulanger & Idriss (2014) cannot be made. However, the Boulanger & Idriss (2014) case history data was regressed herein and expressed in terms total uncertainty (Figure 28, red lines: C_o = 2.623 and σ_T = 0.524), with the total uncertainty being slightly higher than for the $CRR_{7.5}$ relationship proposed herein.

Regarding expressing the probabilistic $CRR_{7.5}$ relationship in terms of model versus total uncertainty, for most applications where the uncertainties in q_{c1Ncs} and CSR* are expected to be similar to those of the case histories used to develop the CRR curves, there is no advantage expressing $CRR_{7.5}$ curves solely in terms of model uncertainty. However, for large projects, such as the liquefaction risk assessment of the Groningen Gas Field where region-specific Ground Motion Predictive Equations (GMPEs), r_d, MSF, fines content correction factors, *etc.* are being developed, it may be advantageous to express the $CRR_{7.5}$ curves in terms of model uncertain if the uncertainties in the region-specific relationships are expected to differ from the uncertainties in the worldwide case histories used to develop the $CRR_{7.5}$ curves. However, this is only feasible if the regressed case history data is sufficient to constrain $\sigma_{ln(R)}$, otherwise specifying a reasonable value for $\sigma_{ln(R)}$ will require considerable judgement.

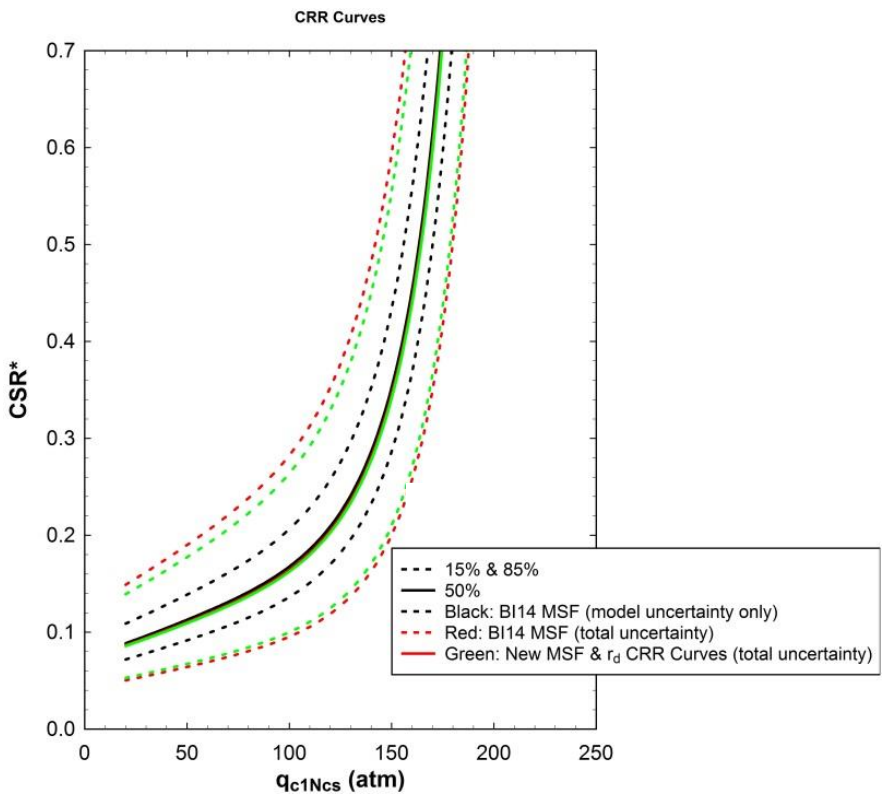

Figure 28. Probabilistic $CRR_{7.5}$ relationships developed herein (green lines) and proposed by Boulanger & Idriss (2014) (black lines). Because these two relationships account for different uncertainties (This Study: total uncertainty; BI14: model uncertainty), the Boulanger & Idriss (2014) data was re-regressed to express the BI14 relationship in terms of total uncertainty (red lines).

6. Summary

Due to issues with r_d and MSF used in the Idriss & Boulanger (2008) and Boulanger & Idriss (2014) liquefaction triggering evaluation procedures, these procedures are not suitable for direct use to evaluate the liquefaction hazard in Groningen. Additionally, these issues are systemic and cannot be simply corrected for. These issues are particularly significant for Groningen because the earthquakes induced from the gas extraction operations have small magnitudes and the associated motions have very different characteristics than those from tectonic earthquakes. As a result, new r_d and MSF relationships were developed herein. These new relationships were used to re-analyse the liquefaction case history database compiled by Boulanger & Idriss (2014) to develop new "unbiased" deterministic and probabilistic $CRR_{7.5}$ relationships; in re-analysing the case history data, all other aspects of the Boulanger & Idriss (2014) procedure were used unchanged (*e.g.*, correction factors for penetration resistance).

To assess the efficacy of the new r_d and MSF relationships versus those proposed by Boulanger & Idriss (2014), the extensive case history data from the 2010-2011 Canterbury, New Zealand, earthquake sequence and 280 worldwide case histories were analysed. The results of this effort showed that the efficacy of the two sets of r_d and MSF relationships is essentially the same. However, while the number of case histories analysed was large, they only represent a relatively limited range in earthquake magnitudes. To assess the efficacy of the two MSF relationships for small magnitude events, more relevant to the Groningen Gas Field, excess pore pressure data from the Wildlife Liquefaction Array and the Gardner Valley Downhole Array were analysed. These results, while limited in number, showed that the new MSF relationship predicted results that are in better accord with field measurements than the Boulanger & Idriss (2014) relationship did. Further assessment of the relative efficacy of the two sets of r_d and MSF relationships may be gained from the data currently be collected and analysed from the **M** 5.7 Valentine's Day earthquake that impacted Christchurch, New Zealand, on 14 February 2016. The significance of this event is that intensity of shaking across Christchurch ranged from low to moderate, potentially allowing the threshold level of shaking required to trigger liquefaction to be constrained.

To evaluate when the two sets of MSF and r_d relationships yield different predictions, the ratio of the factors of safety against liquefaction, FS_{liq}, computed using the new MSF and r_d relationships proposed herein and those proposed by Boulanger & Idriss (2014) were computed for a range of scenarios (*i.e.*, range of earthquake magnitudes, peak ground accelerations, soil densities, and critical depths to liquefaction). For loose sandy soil, there is a monotonic increase in the FS_{liq} ratio for increasing a_{max} and z_{liq}, and a monotonic decrease in FS_{liq} ratio for increasing earthquake magnitude. For the majority of the scenarios, the FS_{liq} computed using the Boulanger & Idriss (2014) over predicts liquefaction susceptibility, relative to when the new MSF and r_d relationships proposed herein are used. This trend becomes more pronounced as a_{max} increases and even more so as the depth to liquefaction increases. For larger magnitude events and lower a_{max}, the FS_{liq} ratio is less than one, implying that the new r_d and MSF relationships result in a lower FS_{liq} than those proposed by Boulanger & Idriss (2014). However, for cases where a_{max} is small, the maximum shear strain induced in the soil by the earthquake shaking should be computed and compared to the threshold strain required to generate residual excess pore water pressures (Dobry *et al.,* 1982). If the maximum induced shear strain at a given depth in a soil profile does not exceed a threshold value (*i.e.,* $\gamma \sim 0.01\%$), residual excess pore pressures will not be generated, and thus, liquefaction will not be triggered regardless of the FS_{liq} computed using a stress-based liquefaction evaluation procedure.

As the density of the soil increases, the influence of the Boulanger & Idriss (2014) MSF's dependency on soil density has a more pronounced effect, resulting in a reduction in the FS_{liq} ratios relative to those for looser soils. However, for many of the scenarios where the FS_{liq} ratio is less than one (implying that the new r_d and MSF relationships result in a lower FS_{liq} than those proposed by Boulanger & Idriss (2014)), the density of the soil is such that liquefaction susceptibility is low and the FS_{liq} computed with either set of MSF and r_d relationships is much greater than 1.0.

7. References

Bates D., M. Maechler, B. Bolker, & S. Walker (2014). lme4: Linear mixed-effects models using Eigen and S4. R package version 1.1-7.

Biondi, G., E. Cascone, & M. Maugeri (2004). Number of Uniform Stress Cycles Equivalent to Seismic Loading. *Proc. 11th Intern. Conf. Soil Dynamics and Earthquake Engrg. and 3rd Intern. Conf. Earthquake Geotech. Engrg.* 2, 705-712.

Booker, J.R., M.S. Rahman, & H.B. Seed (1976). GADFLEA - A computer program for the analysis of pore pressure generation and dissipation during cyclic or earthquake loading. Rep. No. EERC 76-24, Earthquake Engineering Research Center, Univ. of California at Berkeley, Berkeley, CA.

Boulanger, R.W. & I.M. Idriss (2014). *CPT and SPT based liquefaction triggering procedures*. Report No. UCD/CGM-14/01, Center for Geotechnical Modeling, Department of Civil and Environmental Engineering, University of California at Davis, 134 pp.

Bradley, B.A. (2011). Correlation of significant duration with amplitude and cumulative intensity measures and its use in ground motion selection. *Journal of Earthquake Engineering* **15**(6), 809-832.

Carter, W.L., R.A. Green, B.A. Bradley, & M. Cubrinovski (2014). The Influence of Near-Fault Motions on Liquefaction Triggering during the Canterbury Earthquake Sequence. *Soil Liquefaction during Recent Large-Scale Earthquakes* (R.P. Orense, I. Towhata, N. Chouw, eds.), CRC Press, Leiden, The Netherlands, 57-68.

Cetin, K.O. (2000). *Reliability-based assessment of seismic soil liquefaction initiation hazard*. Ph.D. Thesis, University of California, Berkeley.

Cetin, K.O., R.B. Seed, A. Der Kiureghian, K. Tokimatsu, L.F. Harder, R.E. Kayen, & R.E.S. Moss (2004). Standard penetration test-based probabilistic and deterministic assessment of seismic soil liquefaction potential. *Journal of Geotechnical and Geoenvironmental Engineering* ASCE **130**(12), 1314-1340.

Chiou, B., R. Darragh, N. Gregor, & W. Silva (2008). NGA Project Strong-Motion Database. *Earthquake Spectra* EERI **24**(1), 23-44.

Darendeli, M.B. & K.H. Stokoe II (2001). Development of a new family of normalized modulus reduction and material damping curves. Geotechnical Engineering Report GD01-1, University of Texas at Austin, Austin, TX.

DeAlba, P., H.B. Seed, & C.K. Chan (1976). Sand liquefaction in large scale simple shear tests. *Journal of the Geotechnical Engineering Division* ASCE **102**(GT9), 909–27.

Dobry, R., R.S. Ladd, F.Y. Yokel, R.M. Chung, & D. Powell (1982). *Prediction of Pore Water Pressure Buildup and Liquefaction of Sands during Earthquakes by the Cyclic Strain Method.* NBS Building Science Series 138, National Bureau of Standards, Gaithersburg, Maryland.

Efron, B. & R.J. Tibshirani (1994). *An Introduction to the Bootstrap (Vol. 57)*. CRC Press Chicago.

Fawcett, T. (2005). An introduction to ROC analysis. Pattern Recognition Letters **27**, 861-874.

Green, R.A., M. Cubrinovski, B. Cox, C. Wood, L. Wotherspoon, B. Bradley, & B. Maurer (2014). Select liquefaction case histories from the 2010-2011 Canterbury earthquake sequence. *Earthquake Spectra* EERI **30**(1), 131-153.

Green, R.A. & J. Lee (2006). Computation of number of equivalent strain cycles: a theoretical framework. *Geomechanics II: Testing, Modeling, and Simulation* (P.V. Lade and T. Nakai, eds.) ASCE Geotechnical Special Publication 156, 471-487.

Green, R.A., J. Lee, T.M. White, & J.W. Baker (2008). The significance of near-fault effects on liquefaction. *Proceedings of the 14th World Conf. on Earthquake Engineering*, Paper No. S26-019.

Green, R.A., B.W. Maurer, M. Cubrinovski, & B.A. Bradley (2015). Assessment of the relative predictive capabilities of CPT-Based Liquefaction Evaluation Procedures: Lessons Learned from the 2010-2011 Canterbury Earthquake Sequence. *Proc. 6th Intern. Conf. on Earthquake Geotechnical Engineering* (6ICEGE), Christchurch, New Zealand, 2-4 November.

Green, R.A., J.K. Mitchell, & C.P. Polito (2000). An energy-based excess pore pressure generation model for cohesionless soils. *Proceedings of The John Booker Memorial Symposium – Developments in Theoretical Geomechanics* (D.W. Smith and J.P. Carter, eds.), A.A. Balkema, Rotterdam, The Neatherlands, 383-390.

Green, R.A. & G.A. Terri (2005). Number of equivalent cycles concept for liquefaction evaluations - revisited. *Journal of Geotechnical and Geoenvironmental Engineering* ASCE **131**(4), 477-488.

Hancock, J. & J.J. Bommer (2005). The effective number of cycles of earthquake ground motion. *Earthquake Engineering and Structural Dynamics* **34**, 637-664.

Hauksson, E., J. Stock, R. Bilham, M. Boese, X. Chen, E.J. Fielding, J. Galetzka, K.W. Hudnut, K. Hutton, L.M. Jones, H. Kanamori, P.M. Shearer, J. Steidl, J. Treiman, S. Wei, & W. Yang (2013). Report on the August 2012 Brawley Earthquake Swarm in Imperial Valley, Southern California. *Seismological Research Letters* SSA 84(2), 177-189.

Idriss I.M. (1999). An update to the Seed-Idriss simplified procedure for evaluating liquefaction potential. *Proc., TRB Workshop on New Approaches to Liquefaction*, Publication No. FHWA-RD-99- 165, Federal Highway Administration.

Idriss, I.M. & R.W. Boulanger (2008). *Soil Liquefaction during Earthquakes*, Monograph MNO-12, Earthquake Engineering Research Institute, Oakland, CA, 261 pp.

Iwasaki, T., F. Tatsuoka, K. Tokida, & S. Yasuda (1978). A practical method for assessing soil liquefaction potential based on case studies at various sites in Japan. *Proceedings of the 2nd International Conference on Microzonation*, San Francisco, CA, USA, 885-896.

Jones E., E. Oliphant, P. Peterson, *et al.* (2001). *SciPy: Open Source Scientific Tools for Python*, http://www.scipy.org/ [Online; accessed 2015-05-18]

Juang, C.H., T. Jiang, & R.D. Andrus (2002). Assessing probability-based methods for liquefaction potential evaluation. *Journal of Geotechnical and Geoenvironmental Engineering* ASCE **128**(7), 580-589.

Kayen, R., R.E.S. Moss, E.M. Thompson, R.B. Seed, K.O. Cetin, A. Der Kiureghian, Y. Tanaka, & K. Tokimatsu (2013). Shear-wave velocity–based probabilistic and deterministic assessment of seismic soil liquefaction potential. *Journal of Geotechnical and Geoenvironmental Engineering* ASCE **139**(3), 407–419.

Kokusho, T. & Y. Kaneko (2014). Dissipated & strain energies in undrained cyclic loading tests for liquefaction potential evaluations. *Proceedings of the Tenth US National Conference on Earthquake Engineering*, July 21-25, 2014, Anchorage, Alaska, DOI: 10.4231/D3DR2P89D

Lasley, S.J., R.A. Green, & A. Rodriguez-Marek (2016). A New Stress Reduction Coefficient Relationship for Liquefaction Triggering Analyses. *Journal of Geotechnical and Geoenvironmental Engineering* ASCE, *in press*.

Liao, S.S.C. & R.V. Whitman (1986). 'Catalogue of liquefaction and non-liquefaction occurrences during earthquakes.' Res. Rep., Dept. of Civ. Engrg., Massachusetts Institute of Technology, Cambridge, MA.

Maurer, B.W., R.A. Green, M. Cubrinovski, & B.A. Bradley (2015a). Fines-content effects on liquefaction hazard evaluation for infrastructure in Christchurch, New Zealand. *Soil Dynamics and Earthquake Engineering* **76**, 58-68.

Maurer, B.W., R.A. Green, M. Cubrinovski, & B.A. Bradley (2015b). Assessment of CPT-Based Methods for Liquefaction Evaluation in a Liquefaction Potential Index (LPI) Framework. *Geotechnique* **65**(5), 328-336.

Moss, R.E.S, R.B. Seed, R.E. Kayen, J.P. Stewart, A. Der Kiureghian, & K.O. Cetin (2006). CPT-based probabilistic and deterministic assessment of in situ seismic soil liquefaction potential, *Journal of Geotechnical and Geoenvironmental Engineering* ASCE **132**(8), 1032–1051.

Papathanassiou, G., A. Mantovani, G. Tarabusi, D. Rapti, & R. Caputo (2015). Assessment of liquefaction potential for two liquefaction prone areas considering the May 20, 2012 Emilia (Italy) earthquake. *Engineering Geology* **189**, 1-16.

Polito, C., R.A. Green, E. Dillon, & C. Sohn (2013). The effect of load shape on the relationship between dissipated energy and residual excess pore pressure generation in cyclic triaxial tests. *Canadian Geotechnical Journal* **50**(9), 1118-1128.

Polito, C.P., R.A. Green, & J. Lee (2008). Pore pressure generation models for sands and silty soils subjected to cyclic loading. *Journal of Geotechnical and Geoenvironmental Engineering* ASCE **134**(10), 1490-1500.

Robertson, P.K. & C.E. Wride (1998). Evaluating cyclic liquefaction potential using the cone penetration test. *Canadian Geotechnical Journal* **35**, 442–459.

Seed, H.B., I.M. Idriss, F. Makdisi, & N. Banerjee (1975). *Representation of irregular stress time histories by equivalent uniform stress series in liquefaction analysis*. *Rep. No. EERC 75-29*, Earthquake Engineering Research Center, College of Engineering, Univ. of California, Berkeley, Calif.

Steidl, J.H. & S.H. Seale (2010). Observations and Analysis of Ground Motion and Pore Pressure at the NEES Instrumented Geotechnical Field Sites. *Proc. Fifth Intern. Conf. on Recent Advances in Geotechnical Earthquake Engineering and Soil Dynamics and Symposium in Honor of Professor I.M. Idriss*, San Diego, CA 24-29 May 2010.

Yoshimi, Y., K. Tokimatsu, O. Kaneko, & Y. Makihara (1984). Undrained cyclic shear strength of dense Niigata sand. *Soils and Foundations* JSSMFE **24**(4), 131-145.

Youd, T.L., I.M. Idriss, R.D. Andrus, I. Arango, G. Castro, J.T. Christian, R. Dobry, W.D.L. Finn, L.F. Harder, M.E. Hynes, K. Ishihara, J.P. Koester, S.S.C. Liao, W.F. Marcuson, III, G.R. Martin, J.K. Mitchell, Y. Moriwaki, M.S. Power, P.K. Robertson, R.B. Seed, & K.H. Stokoe (2001). Liquefaction resistance of soils: Summary report from the 1996 NCEER and 1998 NCEER/NSF workshops on evaluation of liquefaction resistance of soils. *Journal of Geotechnical and Geoenvironmental Engineering* ASCE **127**(4), 297-313.

Appendix A: Ground Motions Used to Develop New r_d and MSF Relationships

Table A1. NGA earthquake ground motions used to develop new r_d and MSF relationships

No.	Name	Event	M_w	PGA	R^*	Mechanism
1	1011_WON095 1011_WON185	Northridge -01	6.69	0.13	20.3	Reverse
2	1012_LA0000 1012_LA0090	Northridge -01	6.69	0.32	19.1	Reverse
3	1021_L04000 1021_L04090	Northridge -01	6.69	0.08	31.7	Reverse
4	1023_L09090 1023_L09000	Northridge -01	6.69	0.17	25.4	Reverse
5	1027_LV1000 1027_LV1090	Northridge -01	6.69	0.08	37.2	Reverse
6	1029_LV3000 1029_LV3090	Northridge -01	6.69	0.09	37.3	Reverse
7	1033_LIT090 1033_LIT180	Northridge -01	6.69	0.07	46.6	Reverse
8	1041_MTW000 1041_MTW090	Northridge -01	6.69	0.17	35.9	Reverse
9	1050_PAC265 1050_PAC175	Northridge -01	6.69	0.41	7.0	Reverse
10	1051_PUL104 1051_PUL194	Northridge -01	6.69	1.43	7.0	Reverse
11	1060_CUC090 1060_CUC180	Northridge -01	6.69	0.06	80.0	Reverse
12	1074_SAN090 1074_SAN180	Northridge -01	6.69	0.09	41.6	Reverse
13	1078_5108-090 1078_5108-360	Northridge -01	6.69	0.25	16.7	Reverse
14	1091_VAS000 1091_VAS090	Northridge -01	6.69	0.14	23.6	Reverse
15	1096_WWJ090 1096_WWJ180	Northridge -01	6.69	0.05	64.7	Reverse
16	1142_IZ1090 1142_IZ1000	Dinar, Turkey	6.4	0.0	250.5	Normal
17	1154_BRS090 1154_BRS180	Kocaeli, Turkey	7.51	0.06	65.5	Strike-Slip
18	1159_ERG090 1159_ERG180	Kocaeli, Turkey	7.51	0.1	142.3	Strike-Slip
19	1165_IZT090 1165_IZT180	Kocaeli, Turkey	7.51	0.2	7.2	Strike-Slip
20	1168_MNS000 1168_MNS090	Kocaeli, Turkey	7.51	0.01	293.4	Strike-Slip
21	1169_MSK000 1169_MSK090	Kocaeli, Turkey	7.51	0.04	55.3	Strike-Slip
22	1172_TKR090 1172_TKR180	Kocaeli, Turkey	7.51	0.04	165.0	Strike-Slip
23	124_A-FLT000 124_A-FLT270	Friuli, Italy-01	6.5	0.03	102.2	Reverse
24	1257_HWA003-W 1257_HWA003-N	Chi-Chi, Taiwan	7.62	0.09	56.1	Reverse-Oblique
25	126_GAZ000	Gazli,	6.8	0.64	5.5	Unknown

	126_GAZ090	USSR				
26	133_B-SRO000 133_B-SRO270	Friuli, Italy-02	5.91	0.1	14.5	Reverse
27	1347_ILA063-N 1347_ILA063-W	Chi-Chi, Taiwan	7.62	0.09	61.1	Reverse-Oblique
28	1352_KAU003-N 1352_KAU003-W	Chi-Chi, Taiwan	7.62	0.02	114.4	Reverse-Oblique
29	139_DAY-LN 139_DAY-TR	Tabas, Iran	7.35	0.35	13.9	Reverse
30	143_TAB-LN 143_TAB-TR	Tabas, Iran	7.35	0.81	2.0	Reverse
31	1440_TAP065-E 1440_TAP065-N	Chi-Chi, Taiwan	7.62	0.03	122.5	Reverse-Oblique
32	1446_TAP077-N 1446_TAP077-W	Chi-Chi, Taiwan	7.62	0.03	119.0	Reverse-Oblique
33	146_G01230 146_G01320	Coyote Lake	5.74	0.12	10.7	Strike-Slip
34	150_G06230 150_G06320	Coyote Lake	5.74	0.4	3.1	Strike-Slip
35	1518_TCU085-E 1518_TCU085-N	Chi-Chi, Taiwan	7.62	0.06	58.1	Reverse-Oblique
36	1529_TCU102-E 1529_TCU102-N	Chi-Chi, Taiwan	7.62	0.24	1.5	Reverse-Oblique
37	155_F-BEV-EW 155_F-BEV-NS	Norcia, Italy	5.9	0.03	nan	Normal
38	1551_TCU138-N 1551_TCU138-W	Chi-Chi, Taiwan	7.62	0.21	9.8	Reverse-Oblique
39	156_F-CSC-EW 156_F-CSC-NS	Norcia, Italy	5.9	0.19	nan	Normal
40	1577_TTN025-E 1577_TTN025-N	Chi-Chi, Taiwan	7.62	0.04	65.8	Reverse-Oblique
41	1585_TTN040-N 1585_TTN040-W	Chi-Chi, Taiwan	7.62	0.03	48.3	Reverse-Oblique
42	1587_TTN042-N 1587_TTN042-W	Chi-Chi, Taiwan	7.62	0.06	65.3	Reverse-Oblique
43	1613_1060-E 1613_1060-N	Duzce, Turkey	7.14	0.04	25.9	Strike-Slip
44	1618_531-E 1618_531-N	Duzce, Turkey	7.14	0.14	8.0	Strike-Slip
45	1619_MDR000 1619_MDR090	Duzce, Turkey	7.14	0.09	34.3	Strike-Slip
46	1626_212V5180 1626_212V5090	Sitka, Alaska	7.68	0.09	34.6	Strike-Slip
47	164_H-CPE147 164_H-CPE237	Imperial Valley-06	6.53	0.18	15.2	Strike-Slip
48	1645_mtwin000 1645_mtwin090	Sierra Madre	5.61	0.23	10.4	Reverse
49	1649_vquez000 1649_vquez090	Sierra Madre	5.61	0.11	39.8	Reverse
50	1691_ANACA000 1691_ANACA270	Northridge -06	5.28	0.01	nan	Reverse
51	1696_HOW060 1696_HOW330	Northridge -06	5.28	0.07	nan	Reverse
52	1709_0GPN00E 1709_0GPN90W	Northridge -06	5.28	0.04	nan	Reverse
53	1715_WON095	Northridge	5.28	0.05	nan	Reverse

	1715_WON185	-06				
54	1718_LITTL090	Northridge	5.28	0.01	nan	Reverse
	1718_LITTL360	-06				
55	1720_MCS025	Northridge	5.28	0.05	nan	Reverse
	1720_MCS115	-06				
56	1727_RANCH180	Northridge	5.28	0.01	nan	Reverse
	1727_RANCH090	-06				
57	1741_Lsm2000	Little Skull	5.65	0.1	24.7	Normal
	1741_Lsm2270	Mtn,NV				
58	1745_Lsm6000	Little Skull	5.65	0.01	100.2	Normal
	1745_Lsm6270	Mtn,NV				
59	1747_Lsm8270	Little Skull	5.65	0.01	98.3	Normal
	1747_Lsm8000	Mtn,NV				
60	1767_12674090	Hector	7.13	0.02	83.4	Strike-Slip
	1767_12674360	Mine				
61	1786_22T04090	Hector	7.13	0.08	61.2	Strike-Slip
	1786_22T04180	Mine				
62	1795_12647090	Hector	7.13	0.08	50.4	Strike-Slip
	1795_12647180	Mine				
63	1836_22161090	Hector	7.13	0.06	42.1	Strike-Slip
	1836_22161360	Mine				
64	1917_02467360	Anza-02	4.92	0.01	nan	Normal-Oblique
	1917_02467090					
65	1942_12116036	Anza-02	4.92	0.06	nan	Normal-Oblique
	1942_12116126					
66	1961_13095026	Anza-02	4.92	0.03	nan	Normal-Oblique
	1961_13095116					
67	1972_RVB090	Anza-02	4.92	0.01	nan	Normal-Oblique
	1972_RVB360					
68	2017_2017090	Gilroy	4.9	0.01	nan	Strike-Slip
	2017_2017360					
69	2019_47006067	Gilroy	4.9	0.23	nan	Strike-Slip
	2019_47006337					
70	2021_57383090	Gilroy	4.9	0.09	nan	Strike-Slip
	2021_57383360					
71	2032_2014090	Gilroy	4.9	0.01	nan	Strike-Slip
	2032_2014180					
72	2046_0438090	Gilroy	4.9	0.02	nan	Strike-Slip
	2046_0438360					
73	2091_ps07039	Nenana Mountain,	6.7	0.01	199.3	Strike-Slip
	2091_ps07309	Alaska				
74	2118_1727090	Denali,	7.9	0.01	239.5	Strike-Slip
	2118_1727360	Alaska				
75	222_B-LMO265	Livermore-	5.42	0.23	nan	Strike-Slip
	222_B-LMO355	02				
76	225_PFT045	Anza (Horse	5.19	0.12	nan	Strike-Slip
	225_PFT135	Canyon)-01				
77	226_TVY045	Anza (Horse	5.19	0.11	nan	Strike-Slip
	226_TVY135	Canyon)-01				
78	2296_ILA063-N	Chi-Chi,	5.9	0.01	80.4	Reverse
	2296_ILA063-W	Taiwan-02				
79	23_GGP010	San	5.28	0.11	nan	Reverse
	23_GGP100	Francisco				
80	2336_TAP077-N	Chi-Chi,	5.9	0.01	140.1	Reverse
	2336_TAP077-W	Taiwan-02				
81	2367_TCU045-E	Chi-Chi,	5.9	0.02	59.4	Reverse

	2367_TCU045-N	Taiwan-02				
82	2396_TCU085-E	Chi-Chi,	5.9	0.01	78.4	Reverse
	2396_TCU085-N	Taiwan-02				
83	2423_TCU129-E	Chi-Chi,	5.9	0.12	28.3	Reverse
	2423_TCU129-N	Taiwan-02				
84	2427_TCU138-N	Chi-Chi,	5.9	0.04	37.3	Reverse
	2427_TCU138-W	Taiwan-02				
85	2439_TTN025-E	Chi-Chi,	5.9	0.01	106.0	Reverse
	2439_TTN025-N	Taiwan-02				
86	2445_TTN040-N	Chi-Chi,	5.9	0.01	80.9	Reverse
	2445_TTN040-W	Taiwan-02				
87	2447_TTN042-N	Chi-Chi,	5.9	0.01	98.8	Reverse
	2447_TTN042-W	Taiwan-02				
88	2601_TCU045-E	Chi-Chi,	6.2	0.01	77.4	Reverse
	2601_TCU045-N	Taiwan-03				
89	2633_TCU085-E	Chi-Chi,	6.2	0.0	103.6	Reverse
	2633_TCU085-N	Taiwan-03				
90	2640_TCU102-E	Chi-Chi,	6.2	0.02	45.4	Reverse
	2640_TCU102-N	Taiwan-03				
91	265_CPE045	Victoria,	6.33	0.57	14.4	Strike-Slip
	265_CPE315	Mexico				
92	2658_TCU129-E	Chi-Chi,	6.2	0.61	12.8	Reverse
	2658_TCU129-N	Taiwan-03				
93	2661_TCU138-W	Chi-Chi,	6.2	0.13	22.1	Reverse
	2661_TCU138-N	Taiwan-03				
94	2677_TTN025-E	Chi-Chi,	6.2	0.01	97.4	Reverse
	2677_TTN025-N	Taiwan-03				
95	2685_TTN040-W	Chi-Chi,	6.2	0.01	75.1	Reverse
	2685_TTN040-N	Taiwan-03				
96	2687_TTN042-N	Chi-Chi,	6.2	0.01	93.6	Reverse
	2687_TTN042-W	Taiwan-03				
97	2805_KAU003-N	Chi-Chi,	6.2	0.01	116.2	Strike-Slip
	2805_KAU003-W	Taiwan-04				
98	283_A-ARI000	Irpinia,	6.9	0.04	52.9	Normal
	283_A-ARI270	Italy-01				
99	284_A-AUL000	Irpinia,	6.9	0.06	9.6	Normal
	284_A-AUL270	Italy-01				
100	285_A-BAG000	Irpinia,	6.9	0.16	8.2	Normal
	285_A-BAG270	Italy-01				
101	286_A-BIS000	Irpinia,	6.9	0.09	21.3	Normal
	286_A-BIS270	Italy-01				
102	2877_TCU102-E	Chi-Chi,	6.2	0.01	64.8	Strike-Slip
	2877_TCU102-N	Taiwan-04				
103	2897_TCU138-N	Chi-Chi,	6.2	0.04	33.6	Strike-Slip
	2897_TCU138-W	Taiwan-04				
104	2919_TTN025-E	Chi-Chi,	6.2	0.02	69.3	Strike-Slip
	2919_TTN025-N	Taiwan-04				
105	292_A-STU000	Irpinia,	6.9	0.29	10.8	Normal
	292_A-STU270	Italy-01				
106	2927_TTN040-N	Chi-Chi,	6.2	0.02	50.8	Strike-Slip
	2927_TTN040-W	Taiwan-04				
107	2929_TTN042-W	Chi-Chi,	6.2	0.03	69.0	Strike-Slip
	2929_TTN042-N	Taiwan-04				
108	293_A-TDG000	Irpinia,	6.9	0.05	59.6	Normal
	293_A-TDG270	Italy-01				
109	295_B-AUL000	Irpinia,	6.2	0.02	29.9	Normal

	295_B-AUL270	Italy-02				
110	296_B-BAG000	Irpinia,	6.2	0.05	19.6	Normal
	296_B-BAG270	Italy-02				
111	297_B-BIS000	Irpinia,	6.2	0.07	14.7	Normal
	297_B-BIS270	Italy-02				
112	2996_HWA003-N	Chi-Chi,	6.2	0.03	50.4	Reverse
	2996_HWA003-W	Taiwan-05				
113	303_B-STU000	Irpinia,	6.2	0.08	20.4	Normal
	303_B-STU270	Italy-02				
114	3139_TAP077-N	Chi-Chi,	6.2	0.01	152.1	Reverse
	3139_TAP077-W	Taiwan-05				
115	3172_TCU045-E	Chi-Chi,	6.2	0.05	73.5	Reverse
	3172_TCU045-N	Taiwan-05				
116	3194_TCU085-E	Chi-Chi,	6.2	0.01	91.8	Reverse
	3194_TCU085-N	Taiwan-05				
117	3202_TCU102-E	Chi-Chi,	6.2	0.05	52.8	Reverse
	3202_TCU102-N	Taiwan-05				
118	3217_TCU129-E	Chi-Chi,	6.2	0.39	38.9	Reverse
	3217_TCU129-N	Taiwan-05				
119	3220_TCU138-N	Chi-Chi,	6.2	0.18	47.5	Reverse
	3220_TCU138-W	Taiwan-05				
120	3241_TTN025-E	Chi-Chi,	6.2	0.04	94.1	Reverse
	3241_TTN025-N	Taiwan-05				
121	3249_TTN040-N	Chi-Chi,	6.2	0.04	67.4	Reverse
	3249_TTN040-W	Taiwan-05				
122	3251_TTN042-W	Chi-Chi,	6.2	0.05	85.2	Reverse
	3251_TTN042-N	Taiwan-05				
123	3325_HWA003-N	Chi-Chi,	6.3	0.03	56.0	Reverse
	3325_HWA003-W	Taiwan-06				
124	3390_ILA063-N	Chi-Chi,	6.3	0.01	84.5	Reverse
	3390_ILA063-W	Taiwan-06				
125	3479_TCU085-E	Chi-Chi,	6.3	0.01	83.4	Reverse
	3479_TCU085-N	Taiwan-06				
126	3489_TCU102-E	Chi-Chi,	6.3	0.05	35.5	Reverse
	3489_TCU102-N	Taiwan-06				
127	3507_TCU129-E	Chi-Chi,	6.3	0.26	24.8	Reverse
	3507_TCU129-N	Taiwan-06				
128	3509_TCU138-N	Chi-Chi,	6.3	0.06	33.6	Reverse
	3509_TCU138-W	Taiwan-06				
129	3532_TTN025-E	Chi-Chi,	6.3	0.02	94.0	Reverse
	3532_TTN025-N	Taiwan-06				
130	3540_TTN040-N	Chi-Chi,	6.3	0.02	68.8	Reverse
	3540_TTN040-W	Taiwan-06				
131	3542_TTN042-N	Chi-Chi,	6.3	0.03	86.4	Reverse
	3542_TTN042-W	Taiwan-06				
132	369_H-SCN045	Coalinga-0	6.36	0.15	27.5	Reverse
	369_H-SCN315	1				
133	43_CSM095	Lytle	5.33	0.07	nan	Reverse-Oblique
	43_CSM185	Creek				
134	443_CEM000	Borah Peak,	5.1	0.02	nan	Normal
	443_CEM090	ID-02				
135	444_HAU000	Borah Peak,	5.1	0.03	nan	Normal
	444_HAU090	ID-02				
136	45_DCF090	Lytle	5.33	0.13	nan	Reverse-Oblique
	45_DCF180	Creek				
137	454_GIL067	Morgan	6.19	0.1	14.8	Strike-Slip

	454_GIL337	Hill				
138	455_G01230	Morgan	6.19	0.08	14.9	Strike-Slip
	455_G01320	Hill				
139	459_G06000	Morgan	6.19	0.28	9.9	Strike-Slip
	459_G06090	Hill				
140	476_LOB050	Morgan	6.19	0.06	45.5	Strike-Slip
	476_LOB320	Hill				
141	49_SAD003	Lytle	5.33	0.03	nan	Reverse-Oblique
	49_SAD273	Creek				
142	495_S1010	Nahanni,	6.76	1.06	9.6	Reverse
	495_S1280	Canada				
143	496_S2240	Nahanni,	6.76	0.38	4.9	Reverse
	496_S2330	Canada				
144	497_S3270	Nahanni,	6.76	0.15	5.3	Reverse
	497_S3360	Canada				
145	501_D-SG3205	Hollister-	5.45	0.06	nan	Strike-Slip
	501_D-SG3295	04				
146	511_ARM270	N. Palm	6.06	0.12	38.4	Reverse-Oblique
	511_ARM360	Springs				
147	512_ATL270	N. Palm	6.06	0.1	52.1	Reverse-Oblique
	512_ATL360	Springs				
148	525_LMR252	N. Palm	6.06	0.05	66.7	Reverse-Oblique
	525_LMR162	Springs				
149	528_H01000	N. Palm	6.06	0.05	54.8	Reverse-Oblique
	528_H01090	Springs				
150	536_ARS270	N. Palm	6.06	0.11	39.1	Reverse-Oblique
	536_ARS360	Springs				
151	537_SIL000	N. Palm	6.06	0.12	17.0	Reverse-Oblique
	537_SIL090	Springs				
152	541_H02000	N. Palm	6.06	0.08	49.1	Reverse-Oblique
	541_H02090	Springs				
153	585_CPE161	Baja	5.5	1.27	nan	Strike-Slip
	585_CPE251	California				
154	59_CSM095	San	6.61	0.02	89.7	Reverse
	59_CSM185	Fernando				
155	63_FTR056	San	6.61	0.09	30.2	Reverse
	63_FTR326	Fernando				
156	631_A-CHL030	Whittier	5.99	0.03	35.2	Reverse-Oblique
	631_A-CHL120	Narrows-01				
157	643_A-WON075	Whittier	5.99	0.04	27.6	Reverse-Oblique
	643_A-WON165	Narrows-01				
158	661_A-ANG000	Whittier	5.99	0.08	36.8	Reverse-Oblique
	661_A-ANG090	Narrows-01				
159	663_A-MTW000	Whittier	5.99	0.16	22.7	Reverse-Oblique
	663_A-MTW090	Narrows-01				
160	67_ISD014	San	6.61	0.01	131.0	Reverse
	67_ISD284	Fernando				
161	703_A-VAS000	Whittier	5.99	0.06	50.4	Reverse-Oblique
	703_A-VAS090	Narrows-01				
162	715_B-MTW000	Whittier	5.27	0.15	nan	Reverse-Oblique
	715_B-MTW090	Narrows-02				
163	72_L04111	San	6.61	0.16	25.1	Reverse
	72_L04201	Fernando				
164	73_L09021	San	6.61	0.14	22.6	Reverse
	73_L09291	Fernando				
165	763_GIL337	Loma	6.93	0.33	10.0	Reverse-Oblique

	763_GIL067	Prieta				
166	765_G01000	Loma	6.93	0.44	9.6	Reverse-Oblique
	765_G01090	Prieta				
167	769_G06000	Loma	6.93	0.16	18.3	Reverse-Oblique
	769_G06090	Prieta				
168	77_PUL164	San	6.61	1.16	1.8	Reverse
	77_PUL254	Fernando				
169	782_MCH000	Loma	6.93	0.07	44.3	Reverse-Oblique
	782_MCH090	Prieta				
170	788_PJH045	Loma	6.93	0.07	73.0	Reverse-Oblique
	788_PJH315	Prieta				
171	789_PTB207	Loma	6.93	0.07	83.4	Reverse-Oblique
	789_PTB297	Prieta				
172	791_SG3261	Loma	6.93	0.07	34.3	Reverse-Oblique
	791_SG3351	Prieta				
173	795_PHT270	Loma	6.93	0.05	76.1	Reverse-Oblique
	795_PHT360	Prieta				
174	797_RIN000	Loma	6.93	0.09	74.1	Reverse-Oblique
	797_RIN090	Prieta				
175	798_TLH000	Loma	6.93	0.06	76.5	Reverse-Oblique
	798_TLH090	Prieta				
176	801_SJTE225	Loma	6.93	0.28	14.7	Reverse-Oblique
	801_SJTE315	Prieta				
177	804_SSF115	Loma	6.93	0.08	63.2	Reverse-Oblique
	804_SSF205	Prieta				
178	809_UC2000	Loma	6.93	0.34	18.5	Reverse-Oblique
	809_UC2090	Prieta				
179	810_LOB000	Loma	6.93	0.46	18.4	Reverse-Oblique
	810_LOB090	Prieta				
180	813_YBI000	Loma	6.93	0.06	75.2	Reverse-Oblique
	813_YBI090	Prieta				
181	828_PET000	Cape	7.01	0.62	8.2	Reverse
	828_PET090	Mendocino				
182	87_SAD003	San	6.61	0.17	30.7	Reverse
	87_SAD273	Fernando				
183	879_LCN260	Landers	7.28	0.72	2.2	Strike-Slip
	879_LCN345					
184	89_TEH090	San	6.61	0.04	63.8	Reverse
	89_TEH180	Fernando				
185	891_SIL000	Landers	7.28	0.05	50.8	Strike-Slip
	891_SIL090					
186	897_29P000	Landers	7.28	0.07	41.4	Strike-Slip
	897_29P090					
187	922_PPC090	Big	6.46	0.03	nan	Strike-Slip
	922_PPC180	Bear-01				
188	925_RCD090	Big	6.46	0.04	nan	Strike-Slip
	925_RCD180	Bear-01				
189	934_SVP090	Big	6.46	0.06	nan	Strike-Slip
	934_SVP360	Bear-01				
190	938_WBR090	Big	6.46	0.08	nan	Strike-Slip
	938_WBR360	Bear-01				
191	943_ACI000	Northridge	6.69	0.05	68.9	Reverse
	943_ACI270	-01				
192	946_ATB000	Northridge	6.69	0.06	46.9	Reverse
	946_ATB090	-01				
193	957_HOW060	Northridge	6.69	0.14	16.9	Reverse

	957_HOW330	-01				
194	989_CHL070	Northridge	6.69	0.21	20.5	Reverse
	989_CHL160	-01				
195	994_0141-270	Northridge	6.69	0.25	23.8	Reverse
	994_0141-360	-01				

* nan implies that the value is not known